Large-Eddy Simulation of the Stratocumulus-Capped Boundary Layer with Explicit Filtering and Reconstruction Turbulence Modeling

XIAOMING SHI, HANNAH L. HAGEN, AND FOTINI KATOPODES CHOW

Department of Civil and Environmental Engineering, University of California, Berkeley, Berkeley, California

GEORGE H. BRYAN

National Center for Atmospheric Research, Boulder, Colorado

ROBERT L. STREET

Department of Civil and Environmental Engineering, Stanford University, Stanford, California

(Manuscript received 6 June 2017, in final form 20 November 2017)

ABSTRACT

Large-eddy simulation (LES) has been an essential tool in the development of theory and parameterizations for clouds, but when applied to stratocumulus clouds under sharp temperature inversions, many LES models produce an unrealistically thin cloud layer and a decoupled boundary layer structure. Here, explicit filtering and reconstruction are used for simulation of stratocumulus clouds observed during the first research flight (RF01) of the Second Dynamics and Chemistry of the Marine Stratocumulus field study (DYCOMS II). The dynamic reconstruction model (DRM) is used within an explicit filtering and reconstruction framework, partitioning subfilter-scale motions into resolvable subfilter scales (RSFSs) and unresolvable subgrid scales (SGSs). The former are reconstructed, and the latter are modeled. Differing from traditional turbulence models, the reconstructed RSFS stress/fluxes can produce backscatter of turbulence kinetic energy (TKE) and, importantly, turbulence potential energy (TPE). The modeled backscatter reduces entrainment at the cloud top and, meanwhile, strengthens resolved turbulence through preserving TKE and TPE, resulting in a realistic boundary layer with an adequate amount of cloud water and vertically coupled turbulent eddies. Additional simulations are performed in the terra incognita, when the grid spacing of a simulation becomes comparable to the size of the most energetic eddies. With 20-m vertical and 1-km horizontal grid spacings, simulations using DRM provide a reasonable representation of bulk properties of the stratocumulus-capped boundary layer.

1. Introduction

Uncertainty in the climate sensitivities of global climate models primarily arises from their representation of low-latitude boundary layer clouds (Dufresne and Bony 2008; Zelinka et al. 2013; Bretherton 2015). Current climate models cannot resolve the turbulent motions driving the formation and evolution of these clouds. Instead, boundary layer processes are parameterized. In contrast, large-eddy simulation (LES) resolves the energetic eddies responsible for most of the transport of momentum, energy, and mass through the cloud-topped boundary layer and has been an essential tool for developing theory and parameterizations for the cloud-topped boundary layer.

Some cloud regimes, however, such as stratocumulus under sharp temperature inversions, are particularly challenging for LES (Bretherton et al. 1999; Stevens et al. 2005). Turbulence in the stratocumulus-capped boundary layer (SCBL) is mainly driven by radiative cooling at cloud top, which reinforces the inversion strength and sharpness. On the time scale of a few hours, an entrainment–liquid flux feedback dominates the response of the SCBL to perturbations—high liquid water flux and entrainment favor thin stratocumulus, which decreases buoyant generation of turbulence until the entrainment rate is reduced sufficiently so that the radiative cooling may again maintain the cloud (Jones et al. 2014; Bretherton and Blossey 2014). In an intercomparison of simulations of the SCBL, Stevens et al. (2005) showed that even at 5-m vertical resolution,

Corresponding author: Xiaoming Shi, shixm@berkeley.edu

DOI: 10.1175/JAS-D-17-0162.1

some LES models produce a too-strong entrainment at the cloud top, leading to a thin stratocumulus layer and a decoupled SCBL, in which radiatively driven turbulence separates from the surface-heating-driven turbulence below, and the SCBL is not well mixed.

LES is known to be sensitive to subfilter-scale (SFS) turbulence parameterizations in addition to other numerical details, such as grid resolution and choice of advection scheme (Bretherton et al. 1999; Stevens et al. 2005; Cheng et al. 2010; Jones et al. 2014; Pedersen et al. 2016; Pressel et al. 2017). Kirkpatrick et al. (2006) applied the dynamic Smagorinsky model (DSM) to the simulation of the SCBL, in which the Smagorinsky coefficient adapts to the local flow conditions, and found improved statistics compared to the simulations using the standard Smagorinsky model with a constant Smagorinsky coefficient. They suggested that improvement primarily resulted from the minimal SFS fluxes at the inversion. Matheou and Chung (2014) assessed a buoyancy-adjusted stretched-vortex SFS model (BASVM) against diverse atmospheric boundary layer conditions, including a stratocumulus-capped boundary layer, and concluded that their simulations using BASVM agreed well with observation and previous simulation results. DSM and BASVM performed well in simulating the SCBL compared to the ensemble mean of the LES results in Stevens et al. (2005), though the cloud layer in those simulations using DSM and BASVM remained thinner than observations.

Small but energetic eddies exist in the region near the capping inversion of SCBL, and they may produce significant backscatter of energy/scalar variance, that is, the transfer of energy/scalar variance from small scales to large scales. The effects of backscatter have been shown to be critical in near-surface regions (Mason and Thomson 1992; O'Neill et al. 2015). The strong, sharp temperature inversion of the SCBL limits the size of eddies in a manner similar to how eddies would be limited near a solid wall. Therefore, backscatter potentially plays a significant role in determining the turbulent mixing near cloud top. Traditional turbulence schemes are entirely dissipative and thus not able to represent backscatter of SFS turbulence. A dynamic eddy-viscosity model can include negative eddy-viscosity coefficients in theory, but in practice, negative values often cause numerical instability and are clipped at zero (e.g., Chow et al. 2005; Basu and Porté-Agel 2006). The BASVM allows for backscatter in general, yet the particular setup and governing equations of Matheou and Chung (2014) eliminated such possibilities.

Here, we apply an explicit filtering and reconstruction turbulence modeling framework (Gullbrand and Chow 2003; Chow et al. 2005) to the simulation of the SCBL observed during the first research flight (RF01) of the Second Dynamics and Chemistry of the Marine Stratocumulus field study (DYCOMS II) and compare results with other LES turbulence closure models. The dynamic reconstruction model (DRM) of turbulence is developed with the definition and application of an explicit filter. It partitions subfilter-scale (SFS) motions into resolvable subfilter scales (RSFSs) and unresolvable subgrid scales (SGSs), with backscatter allowed via its reconstructed RSFS fluxes. Moeng et al. (2010) demonstrated that the RSFS part can improve the representation of total SFS fluxes by using a mixed model in a priori tests. The DRM also has other desirable properties, such as capturing anisotropic motions and responding to other dynamic terms in the governing equations. It is more complex than simple LES turbulence closures such as the Smagorinsky and turbulence kinetic energy (TKE) 1.5-order schemes but less complex than high-order closures such as the Cloud Layers Unified by Binormals (CLUBB) scheme (Larson et al. 2012) and the intermediately prognostic higher-order closure (IPHOC; Cheng and Xu 2008), which are parameterizations based on probability density functions. As explained below, the DRM can help achieve realistic simulations of the SCBL with proper representation of the effects of unresolved turbulence in both momentum and scalar transport even when relatively coarse resolutions are used.

2. Model and methods

a. Turbulence models

The LES code used is the Cloud Model 1 (CM1; release 18), which solves the nonhydrostatic, compressible[1] equations of the moist atmosphere (Bryan and Fritsch 2002). From the governing equation of velocity u_i, the time tendency due to SFS turbulence T_{u_i} is written as

$$T_{u_i} = -\frac{1}{\overline{\rho}}\frac{\partial \overline{\rho}\tau_{ij}}{\partial x_j},$$

where

$$\tau_{ij} = \overline{u_i u_j} - \overline{u}_i\overline{u}_j \tag{1}$$

is the SFS stress and the overline denotes the spatial filter of the LES. The tendencies of scalars from SFS turbulence are defined similarly, with the velocity u_i

[1] Xiao et al. (2015) found that previous versions of the Weather Research and Forecasting (WRF) Model were sensitive to time stepping for the SCBL when variations in moisture are neglected in WRF's acoustic substepping calculations. CM1 does not have this issue.

above replaced by a scalar. For example, the tendency of potential temperature θ due to SFS turbulence T_θ is

$$T_\theta = -\frac{1}{\overline{\rho}}\frac{\partial \overline{\rho}\tau_{\theta j}}{\partial x_j},$$

where the SFS turbulent flux of potential temperature is defined as

$$\tau_{\theta j} = \overline{\theta u_j} - \overline{\theta}\,\overline{u}_j. \tag{2}$$

In an explicit filtering framework, a spatial filter is explicitly applied during computation. This filter is defined as a top-hat filter in our work. For example, the discrete top-hat filter applied to u in one dimension is

$$\overline{u}_i = 0.25u_{i-1} + 0.5u_i + 0.25u_{i+1}, \tag{3}$$

where i temporarily denotes the grid index. Filter widths of $2\Delta x$ are commonly used for horizontal discretization schemes of fourth-order accuracy (Chow and Moin 2003). Because the filter width is larger than the grid spacing, finescale turbulent motions that are smaller than the filter width but larger than the grid spacing can be partially resolved on the grid. These scales can then be partially reconstructed, as explained further below with the dynamic reconstruction model (Carati et al. 2001; Gullbrand and Chow 2003; Chow et al. 2005). An implicit filtering framework, in contrast, assumes that the grid mesh of an LES acts as the spatial filter. In this case, it is not possible to reconstruct any of the filtered velocities, and all of the turbulence contributions are considered to be subgrid scale.

1) SMAGORINSKY MODEL

In the Smagorinsky model (SM; Smagorinsky 1963), the SFS stress is determined with an eddy viscosity K_m and the resolved strain rate tensor, $\overline{S}_{ij} = (\partial\overline{u}_i/\partial x_j + \partial\overline{u}_j/\partial x_i)/2$,

$$\tau_{ij} = -2K_m\overline{S}_{ij}. \tag{4}$$

In CM1, the eddy viscosity is given by

$$K_m = \begin{cases} (C_s\Delta)^2\left[S^2\left(1-\dfrac{\mathrm{Ri}}{\mathrm{Ri}_c}\right)\right]^{1/2} & \mathrm{Ri}/\mathrm{Ri}_c < 1 \\ 0 & \mathrm{Ri}/\mathrm{Ri}_c \geq 1 \end{cases}, \tag{5}$$

in which $C_s = 0.18$ is the Smagorinsky coefficient, $\Delta = (\Delta x\Delta y\Delta z)^{1/3}$ is a measure of the grid size, $S^2 = 2\overline{S}_{ij}\overline{S}_{ij}$ is deformation, and Ri is the Richardson number. The critical Richardson number $\mathrm{Ri}_c = 1/3$, and the factor $(1 - \mathrm{Ri}/\mathrm{Ri}_c)^{1/2}$ is a stability correction (Mason 1985; Wyant et al. 1997) that suppresses SFS turbulent mixing in stable conditions. The above expression of K_m is deduced from the SFS kinetic energy equation by assuming statistically steady state and homogeneous turbulence.

The SFS flux of scalars is determined similarly with an eddy diffusivity K_h. The expression for θ flux, for instance, is

$$\tau_{\theta j} = -K_h\frac{\partial\overline{\theta}}{\partial x_j}, \tag{6}$$

and K_h is simply given by $K_h = K_m/\mathrm{Pr}$, where Pr is the Prandtl number and is set to 1/3.

2) TKE 1.5-ORDER SCHEME

SFS stress and fluxes in the 1.5-order TKE scheme (Deardorff 1980) also have eddy-viscosity- and eddy-diffusivity-based forms as in Eqs. (4) and (6). A prognostic equation for the SFS TKE (denoted e) is used to determine the eddy viscosity and eddy diffusivity with

$$K_m = c_m l e^{1/2}, \tag{7}$$

$$K_h = c_h l e^{1/2}, \tag{8}$$

where c_m and c_h are model coefficients; $l = [(2/3)(e/N_m^2)]^{1/2}$ is a length scale, in which N_m^2 is the squared Brunt–Väisälä frequency. These coefficients and an additional parameter for the dissipation rate of e need be specified to close the SFS TKE equation (for details, see Stevens et al. 1999). In CM1, $c_m = 0.1$ and $c_h = (1 + 2l/\Delta)c_m$. Those parameters are set to ensure SFS mixing is inactive (i.e., $K_m = K_h = 0$) when Ri is larger than 0.25.

3) MIXED MODEL

When a framework based on explicit filtering is employed, the SFS motions are divided into RSFSs and unresolvable SGSs (Carati et al. 2001; Gullbrand and Chow 2003; Chow et al. 2005). The SFS stress is decomposed as follows:

$$\tau_{ij} = \overline{u_i u_j} - \overline{\tilde{u}}_i\overline{\tilde{u}}_j = \underbrace{(\overline{u_i u_j} - \overline{\tilde{u}}_i\overline{\tilde{u}}_j)}_{\tau_{ij}^{\mathrm{SGS}}} + \underbrace{(\overline{\tilde{u}}_i\overline{\tilde{u}}_j - \overline{\tilde{u}}_i\overline{\tilde{u}}_j)}_{\tau_{ij}^{\mathrm{RSFS}}}, \tag{9}$$

where the tilde denotes the effect of discretization and the overline denotes the explicit filter.

The RSFS stresses can be modeled with reconstructed velocities $\tilde{u}_i^*$:

$$\tau_{ij}^{\mathrm{RSFS}} = \overline{\tilde{u}_i^*\tilde{u}_j^*} - \overline{\tilde{u}}_i^*\overline{\tilde{u}}_j^*. \tag{10}$$

Possible approaches for reconstruction include recursive Taylor series expansions (Katopodes et al. 2000)

and the approximate deconvolution method (ADM; Stolz and Adams 1999; Stolz et al. 2001). In this study, we used the ADM approach,

$$\tilde{u}_i^* = \bar{\bar{u}}_i + (I - G)\bar{\bar{u}}_i + (I - G)[(I - G)\bar{\bar{u}}_i] + \ldots, \tag{11}$$

where I is the identity operator and G is the explicit filter. The nth-order reconstruction retains the first $n + 1$ terms on the right-hand side. The zero-order reconstruction includes only the first term; that is, the reconstructed velocity is approximated with the LES grid velocity $\bar{\tilde{u}}_i$. The RSFS term with zero-order reconstruction is commonly known as the scale-similarity component of the mixed model (Bardina et al. 1983). If an eddy-viscosity model is used to represent τ_{ij}^{SGS}, then

$$\tau_{ij} = \underbrace{-2K_m\bar{S}_{ij}}_{\tau_{ij}^{\mathrm{SGS}}} + \underbrace{(\overline{\tilde{u}_i^*\tilde{u}_j^*} - \bar{\tilde{u}}_i^*\bar{\tilde{u}}_j^*)}_{\tau_{ij}^{\mathrm{RSFS}}}. \tag{12}$$

When the SGS stress is modeled with the Smagorinsky model and zero-order reconstruction is used, we obtain the well-known mixed model (MM) of Bardina et al. (1983). Similarly, the SFS flux of a scalar in the MM is composed of a zero-level reconstructed RSFS term and an SGS term using the Smagorinsky model. Take θ, for example, again:

$$\tau_{\theta j} = \underbrace{-K_h\frac{\partial\bar{\theta}}{\partial x_j}}_{\tau_{\theta j}^{\mathrm{SGS}}} + \underbrace{(\overline{\tilde{\theta}^*\tilde{u}_j^*} - \bar{\tilde{\theta}}^*\bar{\tilde{u}}_j^*)}_{\tau_{\theta j}^{\mathrm{RSFS}}}. \tag{13}$$

As in the standard Smagorinsky model, K_h is given by $K_h = K_m/\mathrm{Pr}$.

4) Dynamic reconstruction model

The DRM (Chow et al. 2005) also uses the explicit filtering framework, with a dynamic eddy-viscosity model for the SGS and the possibility of higher-order velocity reconstruction for the RSFS. When zero-order reconstruction is used, it is also called the dynamic mixed model (Zang et al. 1993). The expressions for SFS stress and fluxes with reconstruction are the same as Eqs. (12) and (13) except that the DRM uses the dynamic eddy-viscosity model of Wong and Lilly (1994; DWL) in lieu of the Smagorinsky model. The detailed equation for the dynamic eddy viscosity in DRM is given by Eq. (18) of Chow et al. (2005):

$$K_m = \frac{\langle (L_{ij} - H_{ij})\hat{\bar{S}}_{ij}\rangle}{2\langle (1 - \alpha^{4/3})\hat{\bar{S}}_{ij}^2\rangle}, \tag{14}$$

where

$$L_{ij} = \widehat{\bar{u}_i\bar{u}_j} - \hat{\bar{u}}_i\hat{\bar{u}}_j,$$
$$H_{ij} = (\widehat{\bar{\tilde{u}}_i\bar{\tilde{u}}_j} - \hat{\bar{\tilde{u}}}_i\hat{\bar{\tilde{u}}}_j) - \hat{\tau}_{ij}^{\mathrm{RSFS}},$$

where $\alpha = 2$ is the ratio of test-filter width to grid-filter width. In the equation above, the hat/caret operator denotes a test filter, and the angle brackets denote local averaging. The grid discretization operator (Chow et al. 2005) has been removed in the above equations for succinctness. The explicit filter, test filter, and local averaging used in this study are three-dimensional and the same as those used in Chow et al. (2005). The term L_{ij} also appears in the traditional DWL formulation, and H_{ij} is an additional "correction" term due to the inclusion of the reconstruction terms in the dynamic procedure.

Previous applications of DRM did not consider scalar transport. The eddy diffusivity for scalar fluxes can also be computed with a dynamic approach (DRM-D), as opposed to using a specified Prandtl number (DRM-Pr). In simulations using DRM-D, dynamic modeling is applied to SGS fluxes of potential temperature and total water mixing ratio separately. The dynamic eddy diffusivity of potential temperature is

$$K_h = \frac{\left\langle (L_{\theta j} - H_{\theta j})\dfrac{\partial\hat{\bar{\theta}}}{\partial x_j}\right\rangle}{\left\langle (1 - \alpha^{4/3})\dfrac{\partial\hat{\bar{\theta}}}{\partial x_j}\dfrac{\partial\hat{\bar{\theta}}}{\partial x_j}\right\rangle}, \tag{15}$$

where

$$L_{\theta j} = \widehat{\bar{\theta}\bar{u}_j} - \hat{\bar{\theta}}\hat{\bar{u}}_j,$$
$$H_{\theta j} = (\widehat{\hat{\bar{\theta}}\hat{\bar{u}}_j} - \hat{\bar{\theta}}\hat{\bar{u}}_j) - \hat{\tau}_{\theta j}^{\mathrm{RSFS}}.$$

The dynamic eddy diffusivity for total water mixing ratio can be computed similarly.

The dynamic modeling of SGS scalar fluxes uses multiple dynamic procedures and leads to an increase in computation time. To reduce computation cost, the simpler DRM-Pr option is considered, in which a parameterized turbulent Prandtl number (Pr_t) is used to obtain eddy diffusivities based on the eddy viscosity K_m. The parameterization of Pr_t follows Venayagamoorthy and Stretch (2010):

$$\mathrm{Pr}_t = \mathrm{Pr}_{t0}\exp\left(-\frac{\mathrm{Ri}}{\mathrm{Pr}_{t0}\Gamma_\infty}\right) + \frac{\mathrm{Ri}}{\mathrm{Ri}_{f\infty}}, \tag{16}$$

where $\mathrm{Pr}_{t0} = 0.7$, $\mathrm{Ri}_{f\infty} = 0.25$, and $\Gamma_\infty = \mathrm{Ri}_{f\infty}/(1 - \mathrm{Ri}_{f\infty}) = 1/3$. The eddy diffusivity for all scalars[2] is then given by $K_h = K_m/\mathrm{Pr}_t$. This saves computation time because only the dynamic procedure for K_m is needed. DRM-Pr can also suppress SFS *scalar* mixing in highly stable conditions, because $\mathrm{Pr}_t \to \infty$ as $\mathrm{Ri} \to \infty$, implying $K_h \to 0$. The relation between Pr_t and Ri is supported by observation data (e.g., Wilson and Venayagamoorthy 2015). This explicit effect of stability is a major difference between DRM-Pr and DRM-D, where the latter is certainly affected by stability but does not have such a specific response.

Near-surface eddy size decreases rapidly, making it impossible to resolve important eddies with relatively coarse grid spacing, in particular when using the test filter to determine the dynamic eddy viscosity. For this reason, DRM underpredicts its eddy viscosity in the near-wall region and therefore underpredicts the near-surface stresses (Chow et al. 2005). To ameliorate this problem, we follow Chow et al. (2005), using the near-wall stress model of Brown et al. (2001) to include additional stress terms for the momentum equations near the wall:

$$\tau_{i3,\text{near-wall}} = -\int C_c a(z)\rho|\mathbf{u}_h|u_i\,dz, \tag{17}$$

where $i = 1, 2$, $|\mathbf{u}_h|$ is the horizontal wind speed, C_c is a scaling factor, and $a(z)$ is the shape function. We set $a(z)$ equal to $\cos^2(\pi z/2h_c)$ for $z < h_c$, where h_c is the cutoff height, and zero otherwise. The integration constants are chosen so that $\tau_{i3,\text{near-wall}} = 0$ at $z = h_c$. As used by most of the simulations in Chow et al. (2005), we choose $C_c = 0.5$ and $h_c = 4\Delta x = 140$ m. For the simulations in section 5, h_c remains 140 m even though Δx is varied. No near-wall models are used for scalar fluxes.

DRM has the capability to include high-order reconstruction terms using the ADM approach. These terms on the right-hand side of Eq. (11) usually become successively smaller; thus, the additional benefit of retaining more terms in the deconvolution process in general dwindles as reconstruction order increases. In the main discussion here, we focus on comparing the two versions of DRM using zero-order (one term) reconstruction with other turbulence models. The effects of increasing reconstruction order are discussed in the appendix.

b. Simulation setup

The case studied is the nocturnal marine stratocumulus observed during RF01 of DYCOMS II (Stevens et al. 2003, 2005). The same idealized initial conditions and forcing are used as those described in Stevens et al. (2005). The initial liquid water potential temperature θ_l and total water mixing ratio q_t are prescribed with a quasi-two-layer structure:

$$\theta_l = \begin{cases} 289.0\,\mathrm{K} & z \le z_i \\ 297.5 + (z - z_i)^{1/3} & z > z_i \end{cases},$$

$$q_t = \begin{cases} 9.0\,\mathrm{g\,kg^{-1}} & z \le z_i \\ 1.5\,\mathrm{g\,kg^{-1}} & z > z_i \end{cases},$$

where z_i is the inversion height and initially set to 840 m. Surface sensible and latent heat flux are set as constants at 15 and 115 W m^{-2}, respectively. The net radiative flux F_{rad} is parameterized with a simplified parameterization as

$$F_{\text{rad}} = F_0\,e^{-Q(z,\infty)} + F_1\,e^{-Q(0,z)} + \rho_i c_p D\left[\frac{(z - z_i)^{4/3}}{4} + z_i(z - z_i)^{1/3}\right],$$

where

$$Q(a,b) = \beta\int_a^b \rho q_c\,dz,$$

and q_c is cloud water mixing ratio. The parameters used are $\beta = 85\,\mathrm{m^2\,kg^{-1}}$, $F_0 = 70\,\mathrm{W\,m^{-2}}$, $F_1 = 22\,\mathrm{W\,m^{-2}}$, and $\rho_i = 1.13\,\mathrm{kg\,m^{-3}}$. We define z_i in the simulations as the local position of the $8.0\,\mathrm{g\,kg^{-1}}$ isoline of q_t; $D = 3.75 \times 10^{-6}\,\mathrm{s^{-1}}$ is the prescribed large-scale divergence, and it determines the large-scale subsidence velocity $W = -Dz$. Random perturbations with amplitude of 0.1 K were added to the initial potential temperature field to initialize the resolved turbulent motion.

This case is sensitive to the choice of advection scheme. Results reported in this study use a fifth-order weighted essentially nonoscillatory (WENO) scheme for the advection of momentum and scalars (Borges et al. 2008), since it helps produce high-fidelity simulations for this case, as discussed by Pressel et al. (2017).[3] A couple of other numerical schemes were also tested for this case, but the results are not included here. When an ordinary fifth-order advection scheme is used for

[2] By applying this diffusivity to the mixing of all scalars, we use Pr_t generically to represent the Schmidt numbers for different scalars.

[3] To be precise, though referred to as "fifth order," the effective order of the WENO scheme here is lower than fifth because CM1 uses a staggered grid and the flow is nonlinear. Also, the WENO scheme used by Pressel et al. (2017) is slightly different from the WENO scheme of CM1 in detail but is not expected to produce different results.

both momentum and scalar equations, more cloud water can be maintained in the simulations than using WENO schemes, but artificial oscillations are found near the inversion. When a sixth-order advection is used for the momentum equations and the WENO scheme is used for scalar equations, cloud water is dramatically underestimated with all turbulence models. DRM consistently provides significant improvement over traditional Smagorinsky and TKE models for all these schemes (despite their deficiencies), consistent with the results reported in this paper.

Microphysics processes are represented with a simple scheme by Bryan and Rotunno (2009). This is an ''all or nothing'' saturation scheme, which does not consider SFS variabilities of microphysical processes. Including an SFS condensation model may improve the simulations at coarse resolutions but is beyond the scope of our current study and is not discussed here.

Different vertical grid spacings are employed in the simulations to test the dependence of our results on resolution. Four values, $\Delta z = 5$, 10, 20, and 40 m, are used in the boundary layer. The horizontal resolution of the main simulations is $\Delta x = \Delta y = 35$ m, and the horizontal number of grid points, $n_x = n_y = 96$, is also the same in all simulations. The vertical extent of the domain is 1.5 km. In the top 0.5 km of the domain, the vertical grid spacing is stretched from 5 to 35 m in the $\Delta z = 5$-m run. Because the inversion height is always below 1 km, this stretching in z should not affect the accuracy of the simulations. No grid stretching is used in the coarser-resolution ($\Delta z > 5$ m) runs. All simulations are run for 4 h, the same as Stevens et al. (2005). Later, in section 5, to evaluate the performance of DRM in the ''terra incognita'' of numerical simulations, horizontal resolutions are coarsened to as much as 1 km in the horizontal while using a vertical spacing of 20 m.

The simulations are named based on the turbulence schemes used (Table 1). Besides those mentioned above—SM, TKE, MM, DRM-D, and DRM-Pr—an additional group of simulations is performed with no model (NM) used for the turbulence closure. All our simulations used the high-performance computing resource of the Yellowstone system (Computational and Information Systems Laboratory 2012).

3. Simulation results

In this section, we examine the simulation of the SCBL against in situ observations to demonstrate the effect of the turbulence closure models. Figure 1 shows the temporal evolution of liquid water path (LWP) in all simulations. The gray shading and black dashed line show the multimodel spread and mean from the LES intercomparison by Stevens et al. (2005). Observations suggest a value of LWP close to what is prescribed in the idealized initial condition was maintained during the RF01 of DYCOMS II (Stevens et al. 2003). Stevens et al. (2005) reported that their simulations with reduced cloud-top mixing are the ones that maintain more liquid water than others.

All our simulations here exhibit a ''spinup'' stage of about 1 h during which LWP decreases. The LWP in the runs with TKE and SM turbulence closure schemes and 5-m vertical spacing stabilizes later at about the 50% and 30% levels, respectively, of the initial LWP. In the NM runs without a turbulence mixing scheme, LWP in the simulation with 5-m vertical spacing is significantly larger than that in the corresponding TKE and SM runs, reaching about the 75% level of initial LWP in later hours. The TKE and SM simulations with 5-m vertical spacing exhibit less liquid water than the multimodel mean of the LES intercomparison by Stevens et al. (2005), while the NM simulation exhibits more liquid water. In contrast, in the MM and DRM simulations that include the reconstructed RSFS fluxes and also use 5-m vertical resolution, LWP reaches about 70% or higher levels of initial LWP, substantially more than the simulations using TKE and SM turbulence closures. Among all simulations with the 5-m vertical spacing, DRM-D, DRM-Pr, and NM maintain the most liquid water, with about 50 g m^{-2} at the end of the simulations.

All simulations exhibit some sensitivity to grid resolution. With $\Delta z = 40$ m, every run loses nearly all of its cloud water. Yet with $\Delta z = 20$m, MM and DRM-Pr still maintain more than half of the liquid water of their 5-m-resolution simulations. DRM-D is more sensitive to resolution than DRM-Pr and does not maintain as high a level of cloud water at the 20-m resolution. An important difference between DRM-D, DRM-Pr, and MM is that DRM-D does not have an explicit correction for stability effects in its formulation of eddy diffusivity, but rather, the stability effects are implicit in the formulation of the scheme. Since the scales of energetic turbulence become underresolved at coarse resolutions, where the dynamic approach is less accurate, spurious turbulence mixing could arise from the combination of coarse grid spacing and sharp inversion-layer gradients.

Figure 2 compares the hour-4 mean profiles of cloud water in simulations with in situ measurements. The mixing ratio of cloud water peaks at about 840 m in all the simulations with 5-m vertical grid spacing. Consistent with Fig. 1, DRM-D at 5-m vertical resolution produces the cloud water profile that matches observations best. It maintains the most cloud water from the initial conditions, which are set according to observations. The mixing ratios in all sets of simulations decrease as resolution

TABLE 1. Computational cost of CM1 for the $\Delta z = 5$-m simulations with different turbulence schemes. The "large" time step is set as 1.5 s, which further splits into 24 small acoustic steps in the simulations. The term "core hours" is defined as wall-clock hours times nodes used times cores per node for a simulation. The term "time factor" is calculated with the computing time of NM simulation as reference.

Turbulence model	Description	Computation cost (core hours)	Time factor
NM	No turbulence model	113.0	1.000
SM	Smagorinsky model	114.4	1.012
TKE	Turbulent kinetic energy model	115.4	1.021
MM	Mixed model	119.9	1.061
DRM-D	Dynamic reconstruction model, dynamic version, zero-order reconstruction	139.2	1.232
DRM-Pr	Dynamic reconstruction model, Prandtl number version, zero-order reconstruction	125.8	1.113
DRM-Pr-1	DRM-Pr using first-order reconstruction	130.6	1.155

coarsens, but MM and DRM-Pr runs have weaker dependence on grid spacing, maintaining an accurate cloud layer even at 20-m vertical resolution. The DRM-D run produces much less liquid cloud water than DRM-Pr and MM at the 20-m resolution, possibly because of excessive mixing near the capping inversion at coarse resolutions, as discussed above. The stability corrections in the scalar diffusivities for DRM-Pr and MM limit mixing in this stable region even at coarser resolutions. The NM simulations are also sensitive to resolution. They lose the capability to maintain a realistic cloud layer as grid spacing coarsens. The NM simulations do appear to be better than TKE and Smagorinsky, which are overly diffusive and maintain a thinner cloud layer even at 5-m resolution.

Figure 3 further demonstrates the different cloud structures by plotting instantaneous distributions of

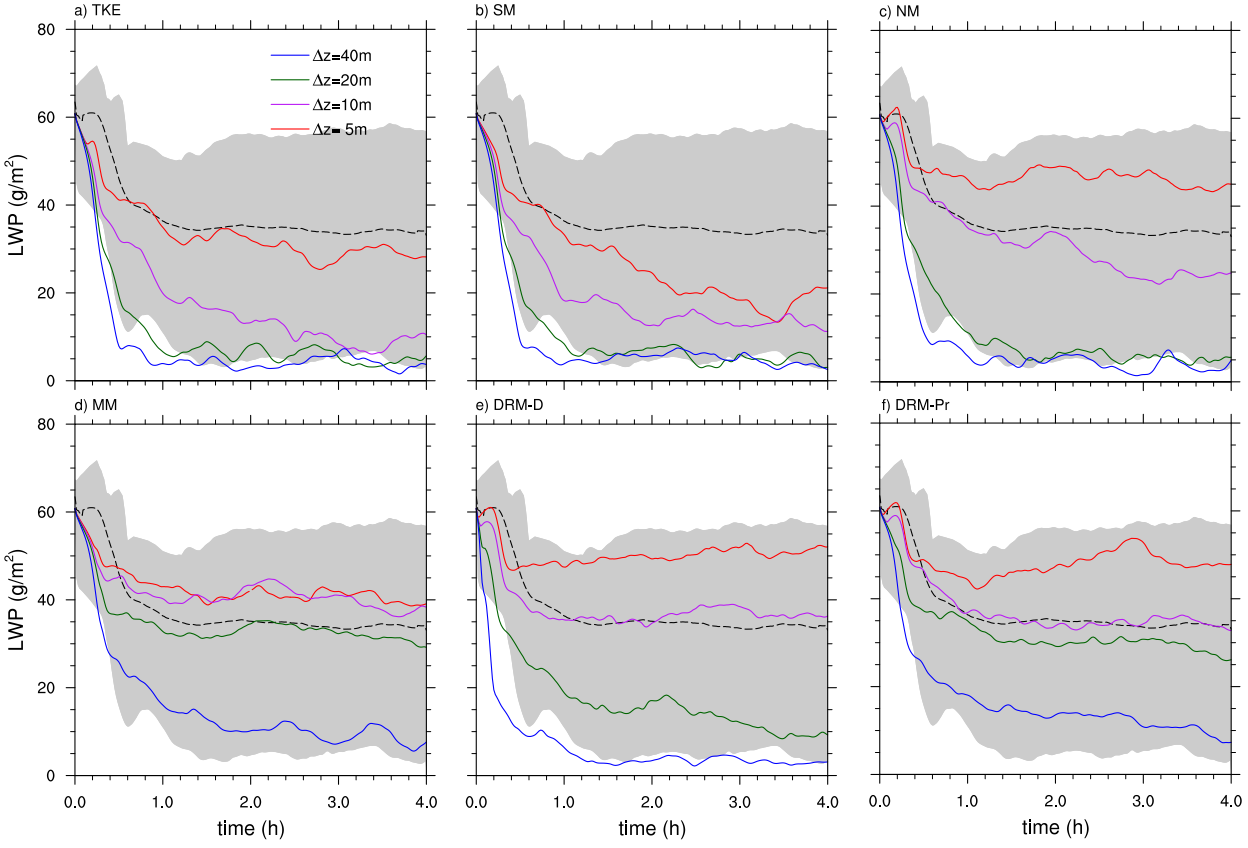

FIG. 1. Time series of LWP for simulations with different turbulence schemes and resolutions. The dashed black curve and gray shading correspond to the ensemble mean and entire distribution of the DYCOMS II RF01 LES intercomparison (Stevens et al. 2005).

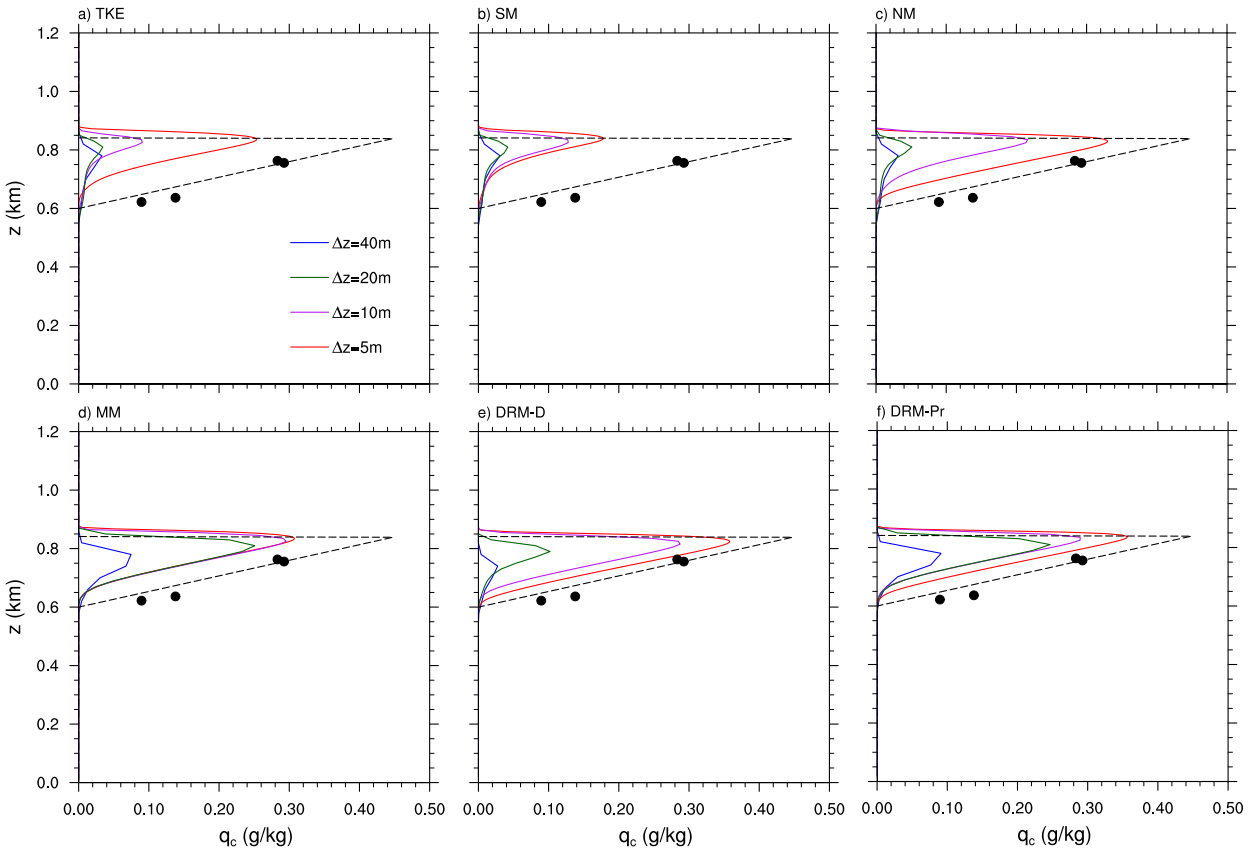

FIG. 2. Hour-4 mean profiles of cloud water mixing ratios q_c for the simulations. The dashed black profile corresponds to q_c from the initial conditions. Solid dots indicate the observed values of q_c during DYCOMS II RF01 (Stevens et al. 2003).

LWP in the simulations with 5-m vertical spacing. The stratocumulus clouds in the TKE and SM runs tend to be broken, whereas the other simulations exhibit a homogeneous cloud layer and nearly 100% cloud cover, consistent with the characteristics of clouds observed during DYCOMS II RF01 (Stevens et al. 2003). Figure 4 shows the evolution of the cloud fraction in the simulations. The TKE and SM simulations have relatively high cloud fractions at 5-m resolution, but less than 100%, while other simulations at 5-m resolution all have 100% cloud cover. As the resolution coarsens, cloud cover deviates from 100% in general. The DRM-D simulation, however, is able to maintain 100% cloud fraction for the 10-m vertical spacing. The MM and DRM-Pr simulations exhibit 100% cloud cover even when Δz is 20 m, at which resolution the TKE, SM, and NM simulations have clearly transitioned away from stratocumulus states.

The SCBL typically exhibits a well-mixed boundary layer below the inversion. Figure 5 shows the profiles of liquid water potential temperature θ_l, which exhibit very small variations with height for all closure models. There are, however, differences above about 0.6 km within the cloud. MM and DRM-Pr show very small differences even down to 20-m resolution. DRM-D shows a bit more warming near the inversion at 20-m resolution, while the remaining runs all exhibit a distinct slightly stable layer above 0.6 km at 20-m resolution. TKE and SM show a slightly warm layer in the upper parts of boundary layer even at 5-m resolution. The less well-mixed states of those simulations suggest a decoupling of the cloud layer and subcloud layer.

The decoupling of the SCBL is more discernible in the mean profiles of total water mixing ratios (Fig. 6). For the TKE and SM simulations, decoupling can be seen at all resolutions. The lower part of the SCBL becomes moister than the observations, while the upper part is drier. This decrease in total water mixing ratio with height is more visible in coarse-resolution simulations. The NM simulation maintains a coupled boundary layer at 5-m vertical resolution but fails to do so at coarser resolutions. The DRM-D simulations perform well at 5- and 10-m vertical resolutions but exhibit decoupling at coarser resolutions. The MM and DRM-Pr are the best

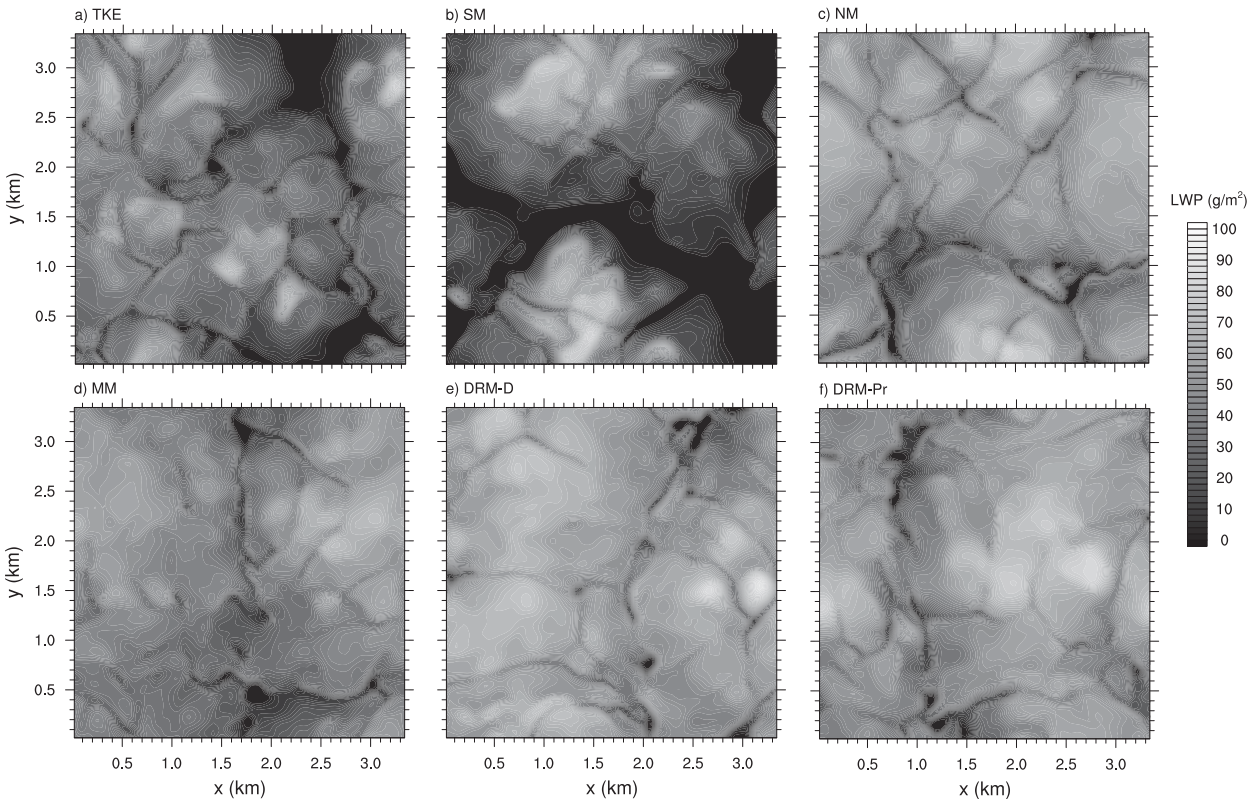

FIG. 3. Snapshots of LWP at the end of the simulations using different turbulence closure schemes. All simulations shown here have a 5-m vertical resolution.

among all simulations, as they can maintain the coupled boundary layer very well down to 20-m resolution. Even when 40-m grid spacing is used, DRM-Pr exhibits a smaller change in total water mixing ratio with height than the others.

The structure of boundary layer turbulence can be reflected by the variance of resolved vertical velocity w (Fig. 7). Observation data exhibit a single well-defined peak in the profile of w variance, implying that the boundary layer is well mixed and that the cloud layer and subcloud layer are coupled by energetic eddies as deep as the boundary layer. The simulations using TKE and SM exhibit double peaks in the profile of w variance, even at 5-m resolution, suggesting a decoupled state. Their maxima are about 40% of the observed maximum and peak within the cloud layer and at about 250 m. The NM run at 5-m resolution exhibits stronger vertical motions and a single peak for the variance of w, but when resolution coarsens, the NM simulations generate double-peak structures. In contrast, the simulations using MM and DRM-Pr exhibit a single peak at vertical resolutions ranging from 5 to 20 m. Their maxima of w variance are located near cloud base, consistent with the observed structure. DRM-D produces w-variance profiles that best match the observations at 5-m resolution; the profiles lose the single-peak structure at 20-m resolution, again probably because of the decreased accuracy of the dynamic procedure at coarse resolutions. For all simulations, strong resolution dependence can be found in the profiles of w variance. This is because the resolved vertical velocity is a filtered quantity, and the coarser-resolution simulations have wider filters. Only in the limit of direct numerical simulation is the resolved w variance expected to match the observed variance exactly.

The third moment of w can also be used to measure the SCBL turbulence structure (Fig. 8). A negative third moment indicates the presence of strong downdrafts as expected in a flow predominantly driven by radiative cooling, whereas a positive third moment tends to indicate surface-heating-driven turbulence and cumulus convection. The TKE and SM simulations are dominated by a positive third moment at low levels of the boundary layer, suggesting decoupled and more surface-driven turbulence in those simulations. In contrast, the NM, MM, and DRM simulations at 5-m resolution all capture the observed negative values of the third moment of w in the cloud layer, implying the flow is driven

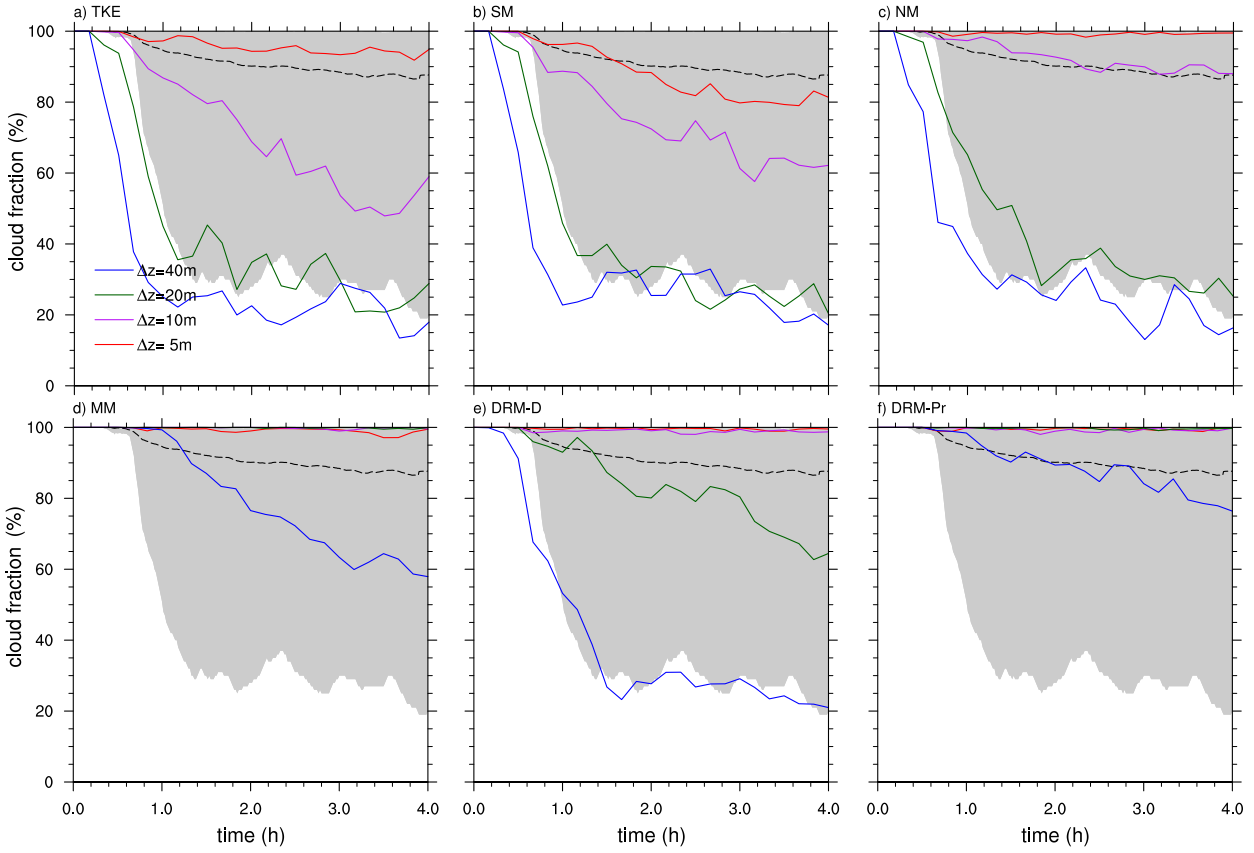

FIG. 4. Time series of cloud fraction for simulations with different turbulence schemes and resolutions. The calculation is based on LWP data, and a model column is defined as "cloudy" if its LWP is greater than 1 g m^{-2}. The dashed black curve and gray shading correspond to the ensemble mean and entire distribution of the DYCOMS II RF01 LES intercomparison (Stevens et al. 2005).

by radiative cooling near cloud top. As the resolution coarsens, the MM and DRM simulations are able to maintain a negative third moment with 10–20-m vertical spacing, but eventually, with 40-m grid spacing, none of the models can maintain it.

In summary, with $\Delta z = 5$ m, DRM-D produces the SCBL with highest fidelity, and the NM simulation without a turbulence model produces more realistic SCBL than the simulations using TKE and SM. At 20-m resolution, MM and DRM-Pr still maintain a single-peaked SCBL turbulence structure and a decent cloud layer, while the other simulations produce a decoupled boundary layer and less LWP. At 40-m resolution, all simulations fail to maintain the cloud layer in SCBL.

Table 1 lists the computing time used by CM1 with different turbulence schemes at the $\Delta z = 5$-m resolution. The reconstruction and dynamic procedures increase computational cost for fixed grid spacings, but as shown later, they improve CM1 simulations of stratocumulus at relatively coarse resolutions, leading to substantial computational savings.

In subsequent sections, we study the effect of the turbulence models by examining the transport of water, heat, and momentum in different simulations.

4. Effects of turbulence models

a. SFS transport of scalars

The entrainment of warm, dry air through the cloud top leads to a reduction of buoyancy when it is mixed with the cold, moist air in clouds driven by radiative cooling. Figure 9a compares the modeled SFS flux of total water in the simulations with 5-m vertical spacing. The upward SFS flux of total water near the inversion is much smaller in DRM-D and DRM-Pr than in other simulations. Within the cloud layer between 600 and 850 m, DRM-D, DRM-Pr, and MM produce significant upward flux of water, whereas TKE and SM have near-zero flux in this layer because the total water is well mixed. Figure 9c shows the total (SFS plus resolved) vertical flux of total water in the entrainment interfacial

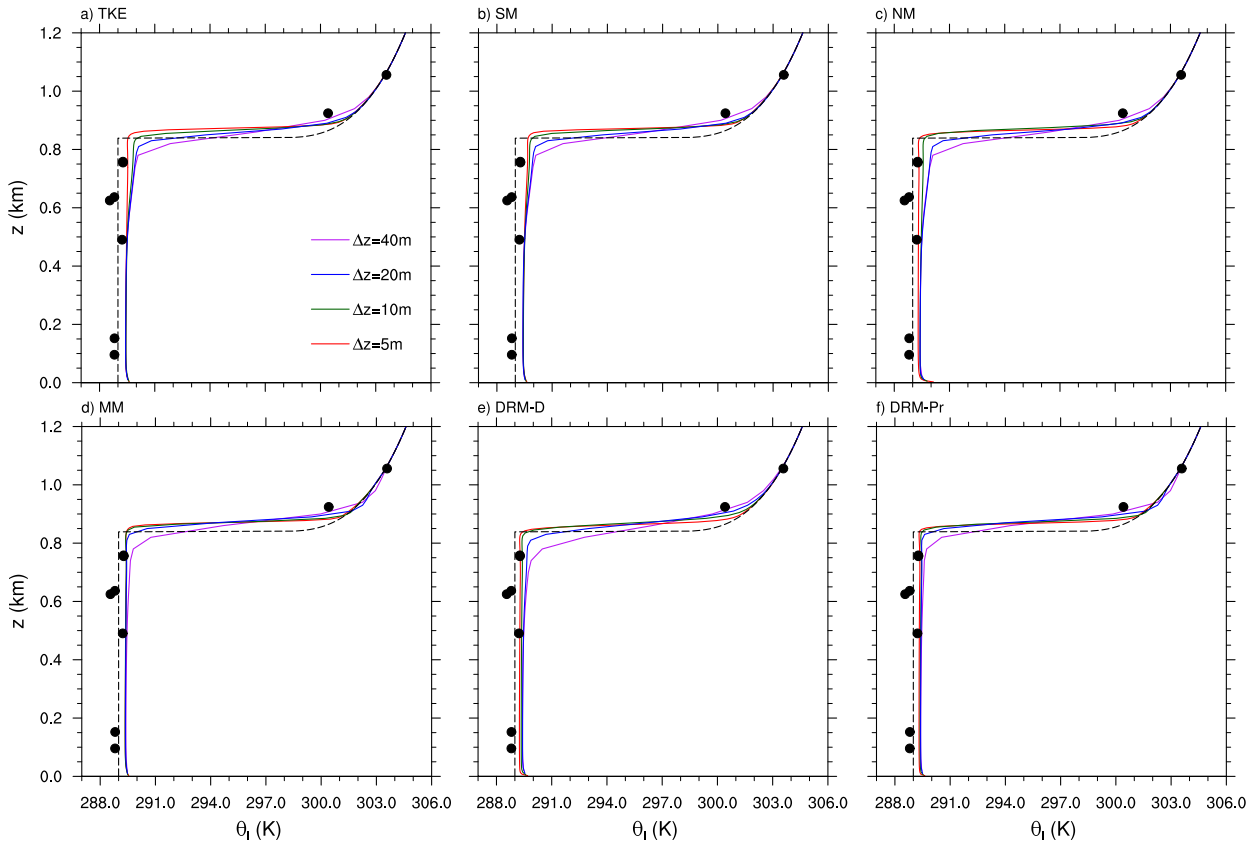

FIG. 5. Hour-4 mean profiles of liquid water potential temperature θ_l for the simulations. The dashed black profile corresponds to θ_l in the initial condition. Solid dots indicate the observed values of θ_l during DYCOMS II RF01.

layer, below which the total flux is dominated by the resolved component. Comparing Figs. 9a and 9c suggests that near the cloud top, however, the modeled SFS flux contributes more than half of the total flux in the TKE, SM, and MM simulations. The resolved component (not shown) in all simulations is actually similar in magnitude near the inversion; thus, the differences in the subfilter components explain why the TKE, SM, and MM simulations have much larger total flux at the cloud top and entrain significantly more dry air there.

Figure 9b shows the modeled SFS θ flux. The two versions of DRM have the smallest downward θ fluxes at the cloud top among all the simulations at 5-m vertical resolution. Figure 9d compares the total θ flux in entrainment interfacial layer. Below this layer, the resolved component dominates the total flux, but within it, the difference in total flux is determined by the SFS component. Again, the resolved flux (not shown) in all simulations is roughly similar in magnitude; thus, the different subfilter components explain why the total θ fluxes in the TKE, SM, and MM simulations are much larger than in others near the inversion, leading to more entrainment of warm air at the cloud top in these simulations. The same conclusion would be reached from profiles of SFS and total fluxes for buoyancy (virtual potential temperature; not shown), which are similar to those for potential temperature in Figs. 9b and 9d.

Stevens et al. (2005) suggested that reducing spurious cloud-top entrainment could improve the simulation of the SCBL; thus, minimal flux of total water and potential temperature is expected in a model capable of simulating a realistic SCBL. This is found in DRM-D and DRM-Pr, which have weaker total water and θ flux than others. The high fidelity of the SCBL simulated with NM with 5-m resolution also supports the view of Stevens et al. (2005), since NM has no explicitly modeled cloud-top mixing (though implicit diffusion due to the numerics still exists). This finding about the high quality of the NM simulation is consistent with the results of Pressel et al. (2017). The NM simulations become inferior, however, when resolutions are coarsened; thus, NM is not a viable option for coarse-resolution simulations of the SCBL.

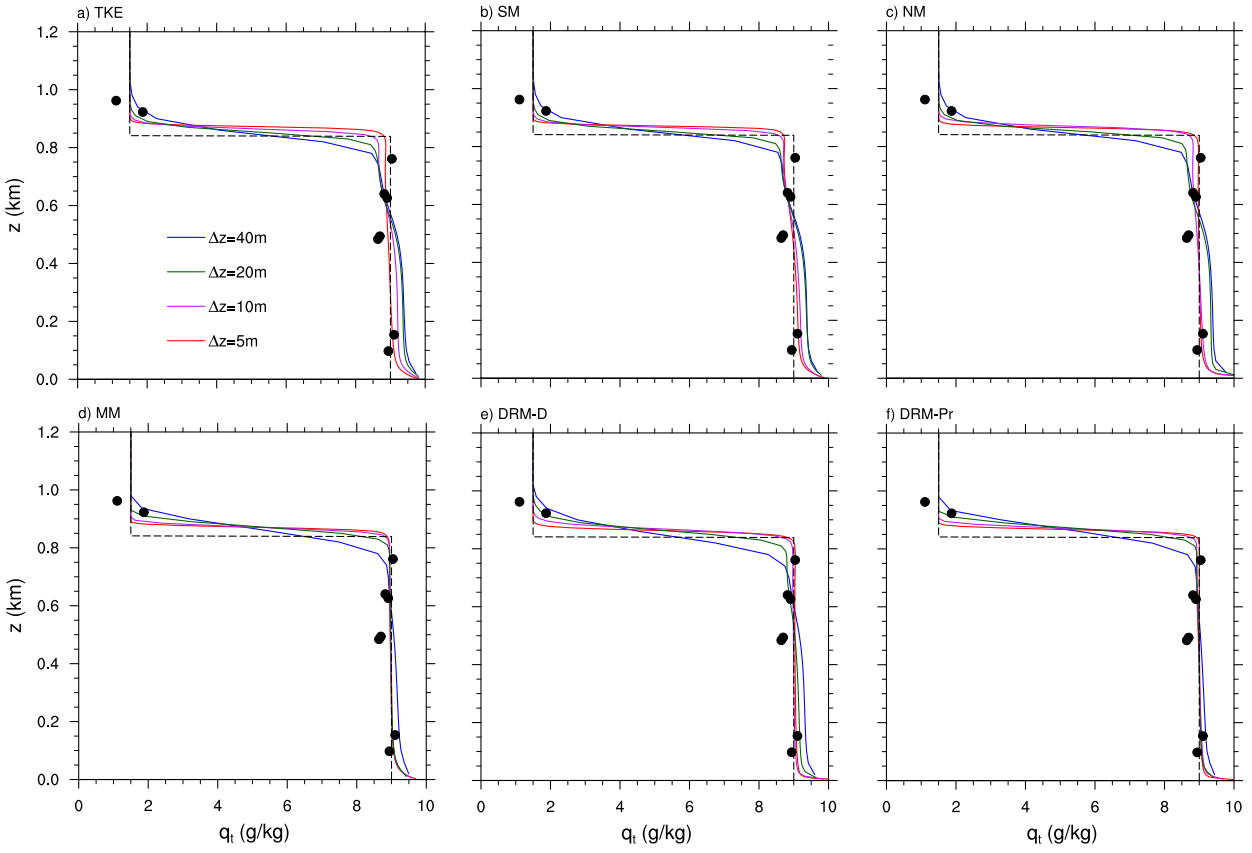

FIG. 6. Hour-4 mean profiles of total water mixing ratio q_t for the simulations. The dashed black profile corresponds to q_t in the initial condition. Solid dots indicate the observed values of q_t during DYCOMS II RF01.

At relatively coarse resolutions, DRM-D also loses its accuracy since the computation of dynamic coefficients relies on the simulation's capability to resolve energetic eddies. Thus, as shown in Figs. 10a and 10b, DRM-D in the simulation with 20-m vertical spacing exhibits significant upward SFS water flux and downward SFS θ flux at the inversion, and the downward SFS θ flux by DRM-D is strongest among all simulations at 20-m resolution. Figures 10c and 10d show total fluxes in these simulations. The resolved flows in those coarse-resolution simulations are not comparable any more since they have diverged to very different boundary layer states; thus, comparing the absolute magnitude of the total flux in the entrainment interfacial layer is not appropriate. In DRM-D, however, the SFS components contribute to a relatively large fraction of total fluxes compared with those in other simulations, especially for the vertical θ flux, confirming this overestimation of SFS fluxes as the cause of DRM-D's deteriorated quality at coarse resolutions.

Following Stevens et al. (2005), it is tempting to conclude that the reduced cloud-top fluxes of θ and water in some simulations are responsible for their realistic boundary layer structures. Figures 9a and 9b, however, show that the potential temperature and water flux at the inversion in the MM run are larger than those in the SM run, while the cloud water profile and w variance in the SM simulation are evidently less realistic than those in the MM run. This suggests that reducing cloud-top entrainment is not the only critical factor in improving simulations of the SCBL. Improving turbulence modeling within the boundary layer, as explained below, seems to be as important as reducing the net cloud-top flux.

The quality of the simulations for the SCBL also depends on the SFS θ flux produced by different turbulence models within the cloud. In Fig. 9, MM, DRM-D, and DRM-Pr produce θ flux that increases with height within the cloud layer and becomes positive at some levels, whereas TKE and SM have downward flux that strengthens with height. Within the cloud, potential temperature increases with height on average; thus, the upward flux means countergradient transport, which cools and destabilizes the corresponding region. The

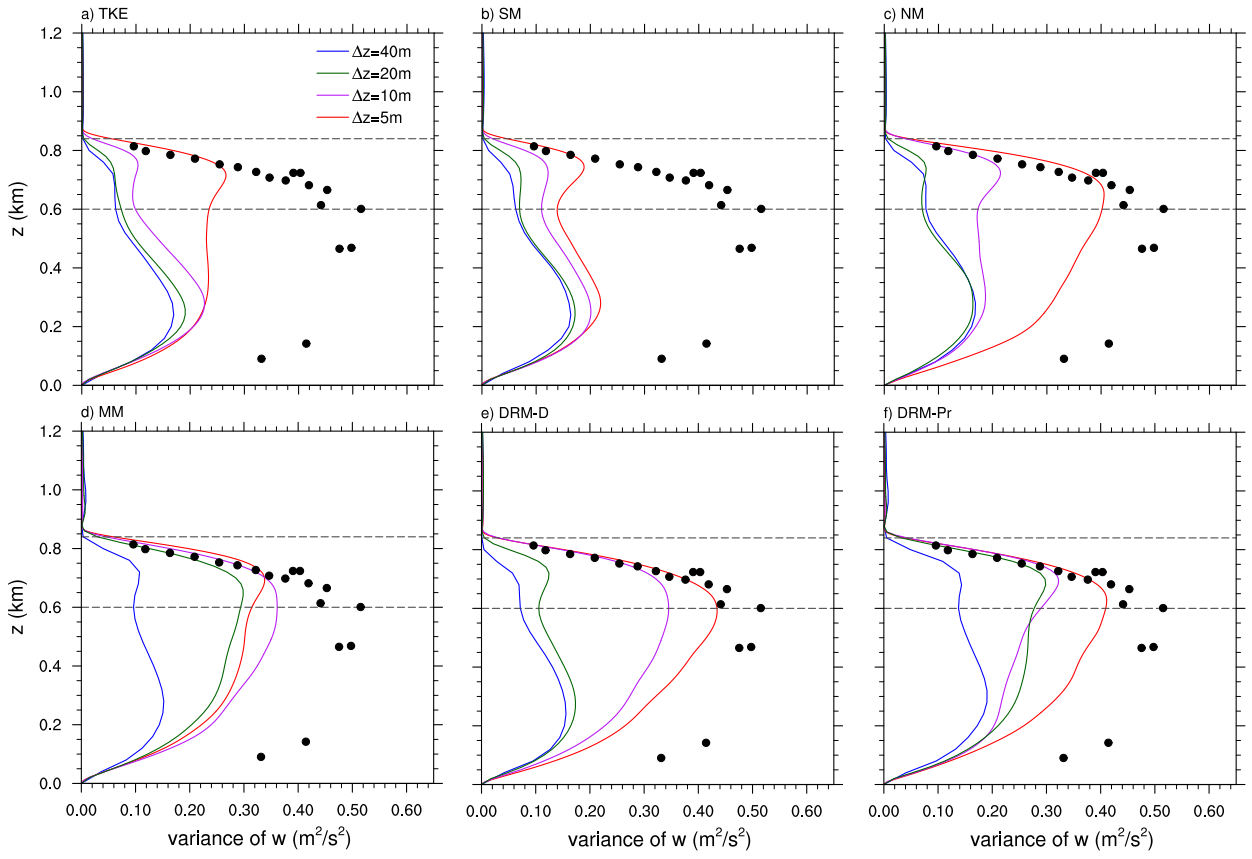

FIG. 7. Hour-4 mean profiles of the variance of resolved vertical velocity $\langle \overline{w}'\overline{w}' \rangle$. Solid dots correspond to the variance of w in observation data. Two dashed black lines indicate cloud base and top in the initial condition.

cooling tendency in the cloud implied by the divergence of mean vertical flux in MM, DRM-D, and DRM-Pr according to Fig. 9 is relatively small, $\sim 0.05\,\mathrm{K\,h^{-1}}$, except for DRM-D near the cloud top at about 850 m ($\sim 0.5\,\mathrm{K\,h^{-1}}$).

The overall influence of SFS mixing on turbulence is three-dimensional; thus, despite the small amplitude of the net in-cloud divergence of θ flux, countergradient transport may still be important. We can better appreciate the effects of SFS mixing by examining the evolution equation for SFS turbulent potential energy (TPE), which reveals how the modeled SFS flux affects the energetics of turbulence:

$$\frac{De_p}{Dt} = -\frac{1}{\overline{\rho}}\frac{\partial}{\partial x_j}(\overline{\rho}\Phi_j) - \tau_{\theta j}\frac{\partial \overline{\theta}}{\partial x_j}, \tag{18}$$

where

$$\Phi_j = \overline{E_p u_j} - \overline{E}_p \overline{u}_j - \overline{\theta}\tau_{\theta j} \tag{19}$$

is a third-order moment and

$$E_p = \frac{\theta^2}{2},$$
$$\overline{E}_p = \frac{\overline{\theta}^2}{2},$$
$$e_p = \frac{(\overline{\theta^2} - \overline{\theta}^2)}{2}$$

are the unfiltered, filter-scale total and SFS turbulent potential energy, respectively; e_p can be called the subfilter-scale TPE because the variance of $\overline{\theta}$ is a measure of TPE at resolved scales (Zilitinkevich et al. 2007). The influences of microphysical and radiative forcings on subfilter-scale TPE are neglected in Eq. (18) for simplicity.

The term that determines the transfer of TPE from resolved scales to subfilter scales is the second term on the right-hand side of Eq. (18), $\Pi_\theta = -\tau_{\theta j}\,\partial\overline{\theta}/\partial x_j$, because the divergence of the third-order moments vanishes if Eq. (18) is integrated in a closed system. A positive value of Π_θ implies downgradient transport of potential temperature, and a negative value of Π_θ implies

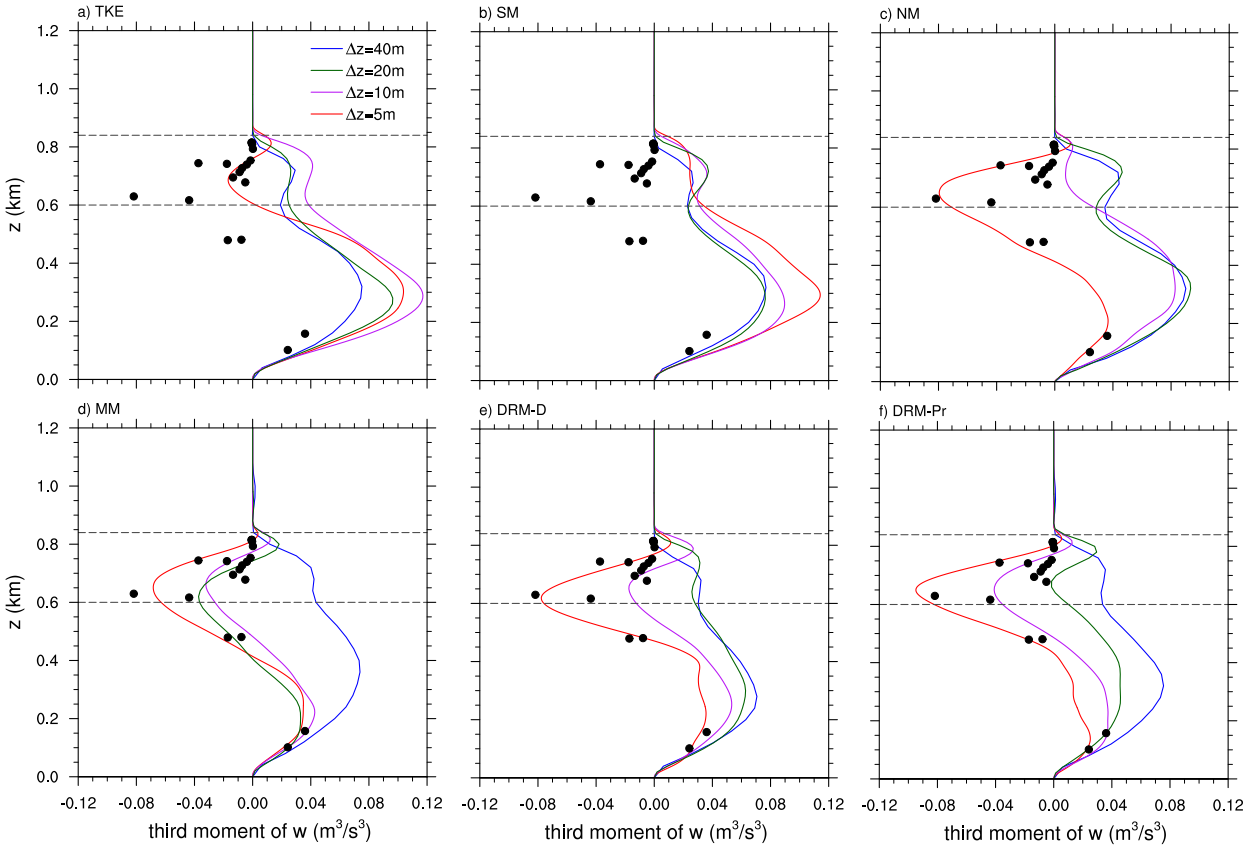

FIG. 8. Hour-4 mean profiles of the third moment of resolved vertical velocity $\langle \overline{w}'\overline{w}'\overline{w}' \rangle$. Solid dots correspond to the third moment of w in observation data. Two dashed black lines indicate cloud base and top in the initial condition.

countergradient transport. The effect of downgradient transport is to smooth the resolved field and reduce resolved-scale variance of θ (TPE), which is, essentially, buoyancy. In a closed system, such diffusion of resolved TPE tends to produce a globally uniform $\overline{\theta}$ field if it is applied to the system alone. In contrast, countergradient transport transfers the variance of θ from SFS to resolved scales, allowing more buoyancy to be kept and converted to resolved kinetic energy. This action can be called backscatter of TPE.

Figure 11a shows the probability distribution function (PDF) of the transfer rate Π_θ in the cloud ($z = 800$ m) in the simulations with 5-m vertical grid spacing. The right half (positive values) indicates the frequency of forward-transfer rates through the term Π_θ, and the left half (negative values) indicates the frequency of backscatter. TKE and SM can only produce forward transfer of TPE (i.e., moving TPE from the resolved scales to subfilter scales). This is because for any eddy-viscosity model, $\Pi_\theta = K_h(\partial\overline{\theta}/\partial x_j)^2 \geq 0$. In contrast, the MM, DRM-D, and DRM-Pr simulations have significant fractions of backscatter. Figure 11b shows the average of the scaled transfer rate, $\Pi_\theta/\sigma_{\Pi_\theta}$, where σ_{Π_θ} is the standard deviation of Π_θ at a given level. The different turbulence closure schemes show the most disparity within the cloud layer. TKE and SM produce positive values of Π_θ in the cloud layer, showing that forward transfer dominates and that these schemes are highly dissipative. DRM-Pr and MM produce near-zero positive values in the cloud, suggesting that they are only weakly diffusive and their influence on turbulence is similar to the NM simulation, which has zero SFS dissipation. DRM-D, on the contrary, exhibits negative values of Π_θ, meaning DRM-D produces net backscatter in the cloud. DRM-D can produce net backscatter because it is the only scheme that computes eddy diffusivity with a dynamic procedure, which produces near-zero eddy diffusivity in the cloud layer (not shown).

The presence of backscatter in cloud seems to be critical, because buoyancy in the SCBL is generated in the upper part of the cloud by radiative cooling. A highly diffusive turbulence model tends to remove buoyancy from the resolved flow before it can be converted to resolved kinetic energy. A backscatter-permitting

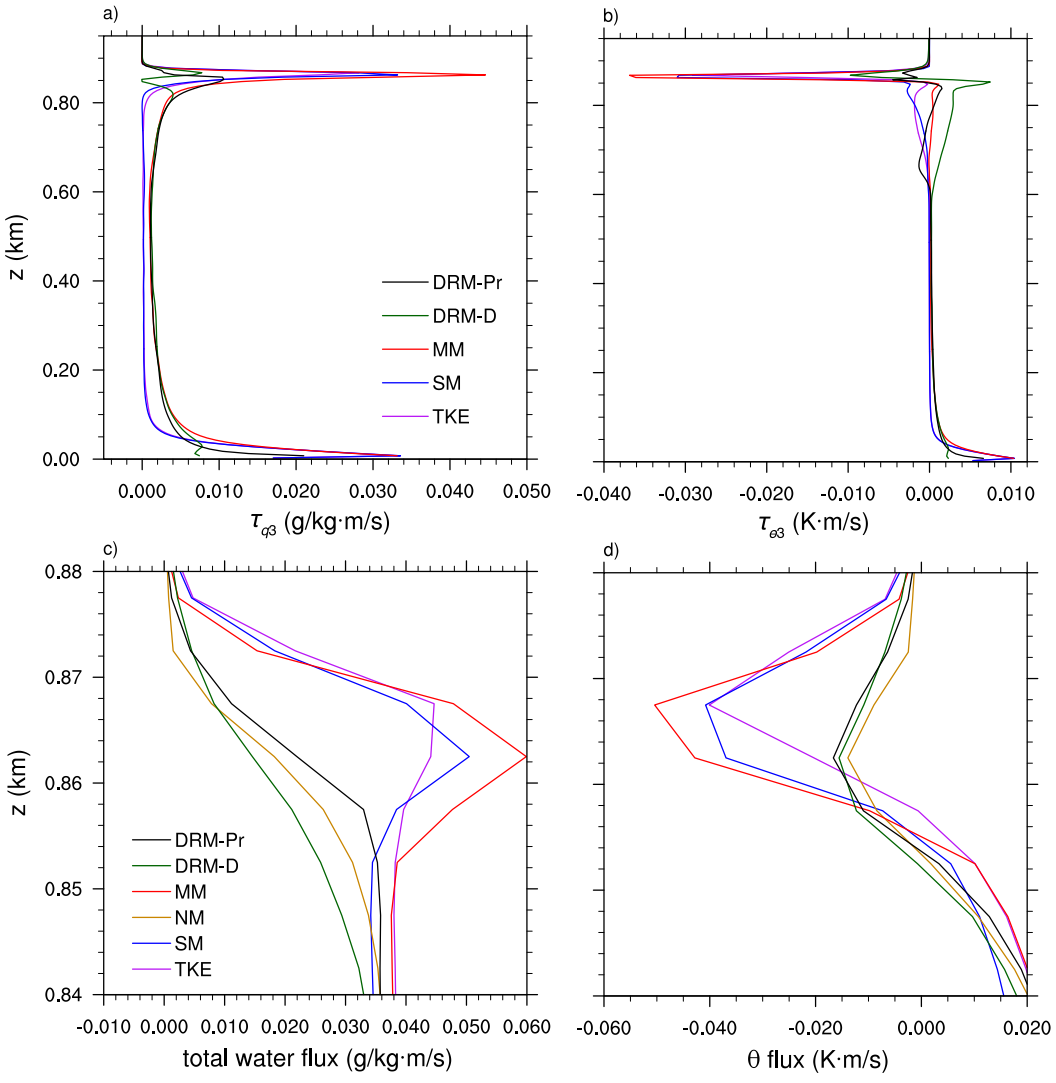

FIG. 9. Hour-4 mean profiles of (a) the modeled SFS vertical flux of total water τ_{q3}, (b) the modeled SFS vertical θ flux $\tau_{\theta 3}$, (c) total (SFS plus resolved; $\langle \overline{w}'\overline{q}_t' + \tau_{q3} \rangle$) vertical flux of total water, and (d) total $\langle \overline{w}'\overline{\theta}' + \tau_{\theta 3} \rangle$ vertical θ flux for the simulations at 5-m vertical resolution.

scheme, however, not only keeps the buoyancy generated by radiative cooling at resolved scales but may also *increase* the local resolved-scale buoyancy when backscatter occurs.

b. SFS transport of momentum

Above, we illustrated how the choice of turbulence model modulates the cross-scale transfer of TPE in LES of the SCBL. Besides affecting TPE, the turbulence closure also directly influences the budget of kinetic energy (KE) through the momentum equation. Similar to Eq. (18), the transfer of global kinetic energy from resolved to SFS motions is determined by a global integral of

$$\Pi = -\tau_{ij}\frac{\partial \overline{u}_i}{\partial x_j} = -\tau_{ij}\overline{S}_{ij},$$

which indicates a local forward transfer of kinetic energy (i.e., dissipation of resolved energy) if $\Pi > 0$ and local backscatter if $\Pi < 0$. In Fig. 12a, again, the right half of the panel indicates the frequency of forward transfer and the left half indicates the frequency of backscatter. The PDF of Π at $z = 800$ m in the cloud is shown in Fig. 12a. MM, DRM-D, and DRM-Pr have notable fractions of backscatter. When averaged horizontally (Fig. 12b), the different simulations exhibit similar rates of dissipation throughout most of the boundary layer but

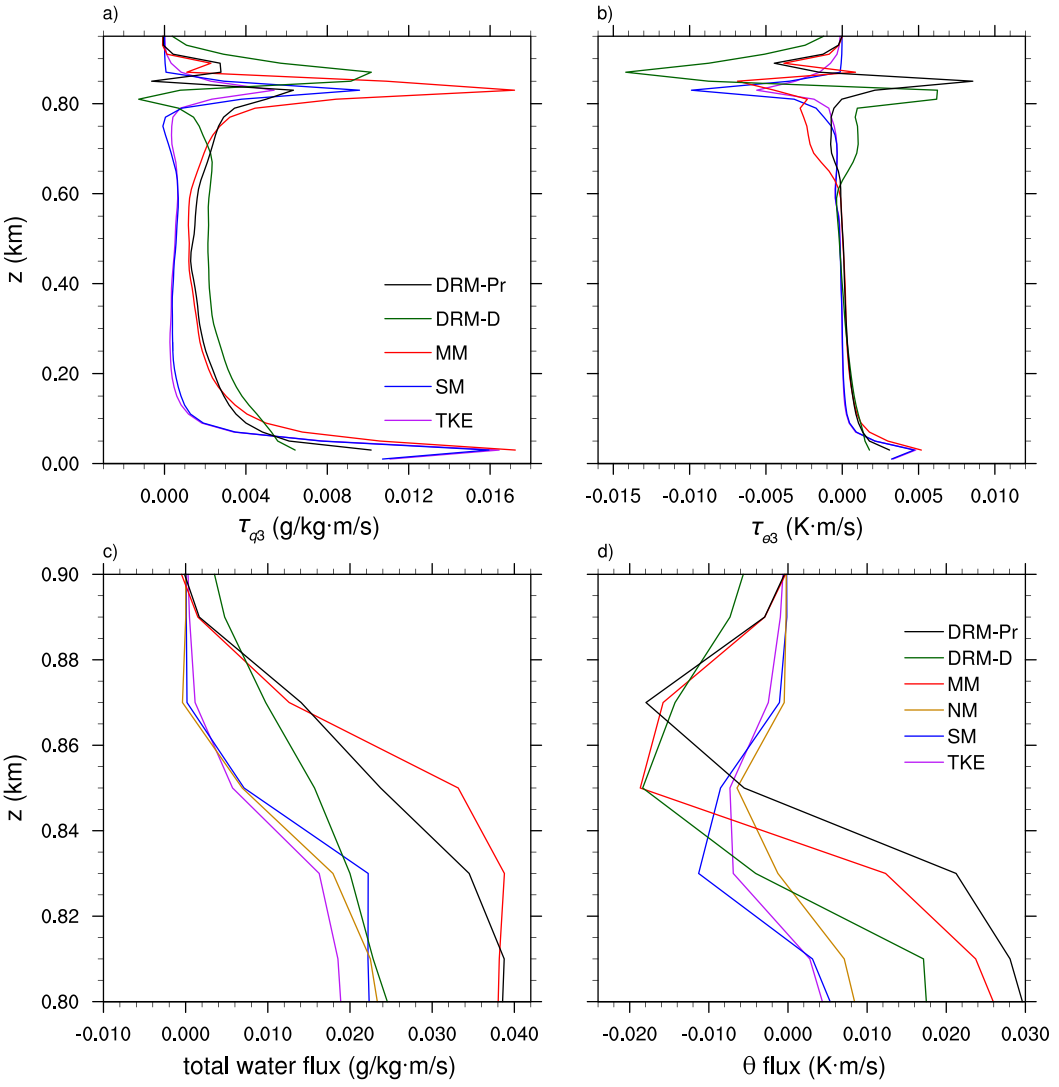

FIG. 10. As in Fig. 9, but for 20-m vertical resolution.

large differences near the surface and above the cloud top, where the models using reconstruction exhibit smaller rates of dissipation.

To quantify the effects of the backscatter of kinetic energy in the simulations, we performed a special group of simulations in which the MM is used for the turbulence closure for momentum but not for scalars. Thus, we retain $\tau_{ij}^{\mathrm{RSFS}}$ in Eq. (12) but discard $\tau_{\theta j}^{\mathrm{RSFS}}$ in Eq. (13) and the reconstructed RSFS fluxes of cloud water and water vapor, using Smagorinsky alone for those fluxes. The mixed model is chosen for this special group of simulations because its SGS model is invariant to changes in the RSFS model. The modeled scalar fluxes can still be indirectly affected by the reconstruction through the resolved strain-rate tensor and stability in Eq. (5), both of which are modified because of the reconstructed momentum flux.

Figure 13 shows the time series of LWP and the variance of vertical velocity in these simulations. Though there are slight decreases compared with the original MM simulations, LWP is still notably larger than with SM, especially in the simulations with 5-m vertical spacing. The vertical velocity variance field shows double peaks in the boundary layer at 5-m resolution, but its amplitude is larger than in the SM simulations, showing a strengthening of turbulence due to the reduced TKE dissipation. However, it is still weaker than the w variance in the original MM simulations, suggesting that turbulence is weakened because of the reduced TPE when SFS scalar fluxes are only modeled with the Smagorinsky term.

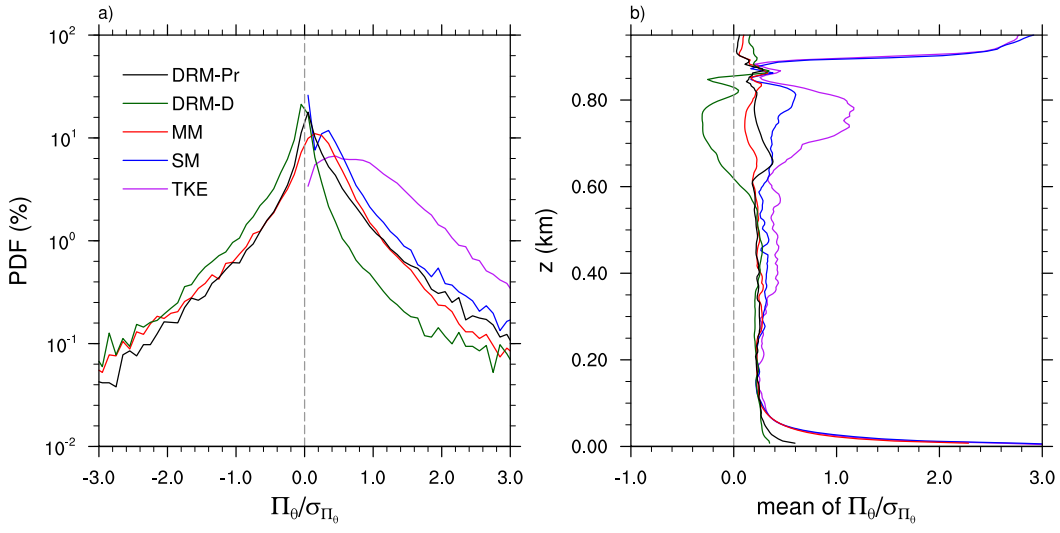

FIG. 11. (a) PDF at $z = 800$ m and (b) the normalized average at all vertical levels for the scaled transfer rate Π_θ, which measures resolved-scale to subfilter-scale transfer of the variance of potential temperature; σ_{Π_θ} is the standard deviation of Π_θ. Data from hour 4 of the simulations are used to compute Π_θ.

Forward and backscatter are dealt with quantitatively in Leslie and Quarini (1979). They show that, while there is a net drain of energy to small scales in a three-dimensional flow on average, instantaneous backscatter occurs. Since the DRM includes a reconstruction part, it follows that the reconstruction will have the same physics as the actual flow (i.e., it will allow backscatter). Since the SGS part is designed to prohibit backscatter, only the reconstructed flux can produce backscatter.

In the cloud, energy is input at relatively small scales through radiative cooling in a narrow region in the upper part of cloud, and the flow is three dimensional. In the actual computation, there is, on average, transport from large to small scales as shown in Figs. 11b and 12b. If the transfer across the explicit filter scale is calculated, then that transfer is the sum of reconstructed RSFS buoyancy production and strain production and modeled SGS diffusion and dissipation. But, at any or many instants, backscatter may be calculated (i.e., negative transfer) as shown by the PDFs in Figs. 11a and 12a. It is hard to verify the accuracy of DRM-D in modeling backscatter without detailed observations or a direct

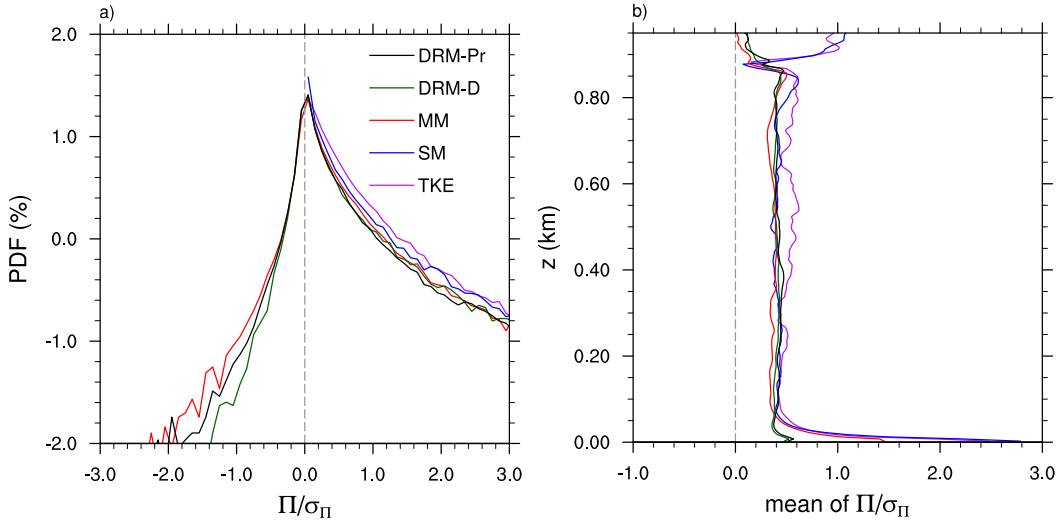

FIG. 12. As in Fig. 11, but the cross-scale transfer rate of kinetic energy is shown.

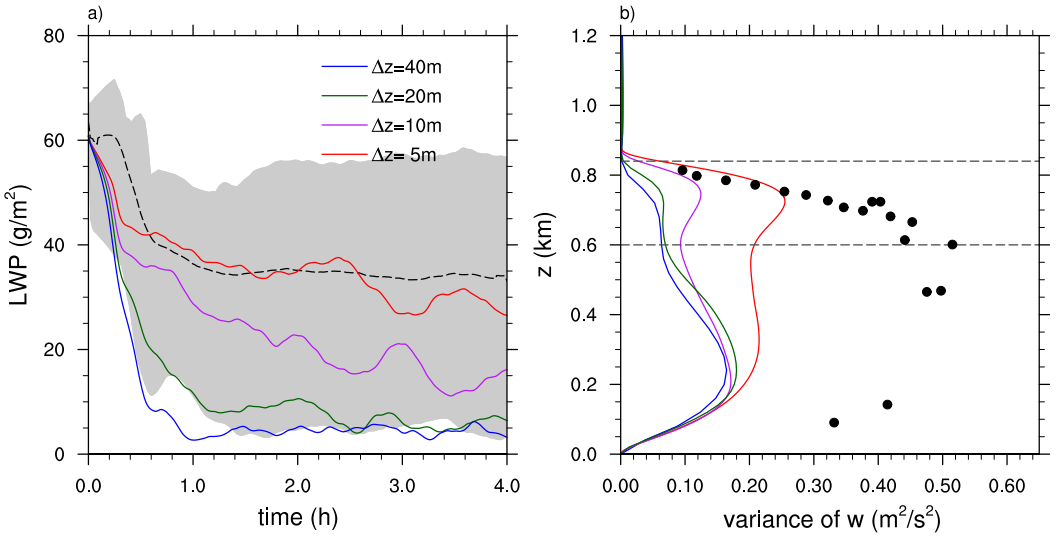

FIG. 13. (a) LWP time series and (b) w variance in simulations that uses the MM for the SFS momentum flux but Smagorinsky for scalar fluxes.

numerical simulation (e.g., de Lozar and Mellado 2015). See also the review and suggestions in Mellado (2017). However, based on the quality of the simulations demonstrated in section 3, we can conclude that DRM-D models the cross-scale transfer of TKE and TPE in a way that is more successful in maintaining cloud water and active turbulence in the LES of SCBL than the traditional eddy-viscosity-based turbulence models.

5. SCBL in the terra incognita

The terra incognita (TI), also known as the gray zone, of numerical simulation refers to a range of grid spacing that is on the order of the scale of energetic turbulence (Wyngaard 2004). Challenges for LES arise in the TI because traditional models for SFS turbulence in LES were designed for grid spacing much smaller than the energy-containing eddies. Pope (2000) provided guidance as to what constitutes LES, indicating that about 80% of the energy should be resolved. Matheou and Chung (2014) wrote that, in their experience, 90% of the TKE must be resolved for the statistical means to be reliable. They then integrated the Kolmogorov spectra to define grid spacings to achieve these goals, yielding the guidance that the grid spacing must be less than 1/12 or 1/32 times the integral scale of the flow (nominally the scale of the spectral peak) to resolve 80% or 90% of the energy, respectively. In the context then of the Wyngaard (2004) definition of TI, we here define TI as the range of grid spacing within or greater than (1/12–1/32)l, where l is the scale of the large eddies in the flow.

The horizontal and vertical large-eddy scales are different in our stratocumulus simulation, as the vertical scale is set roughly by the 200-m-thick cloud layer. To estimate the horizontal eddy scale, we performed a simulation in a large 96 km × 96 km domain with

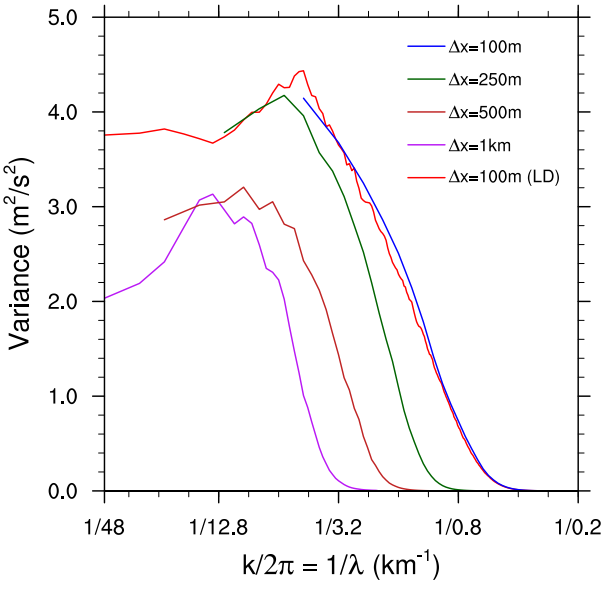

FIG. 14. Spectra of w variance below the inversion; k is the horizontal wavenumber. Vertical velocities are Fourier transformed in x and y directions separately, and then the resulting spectra are averaged over y, x, and z directions. The numbers of grid points $n_x = n_y$ =960 in the horizontal for the LD simulation and $n_x = n_y$ =96 for others. Data from hour 4 are used in the computation, and all simulations shown here used the DRM-Pr turbulence closure.

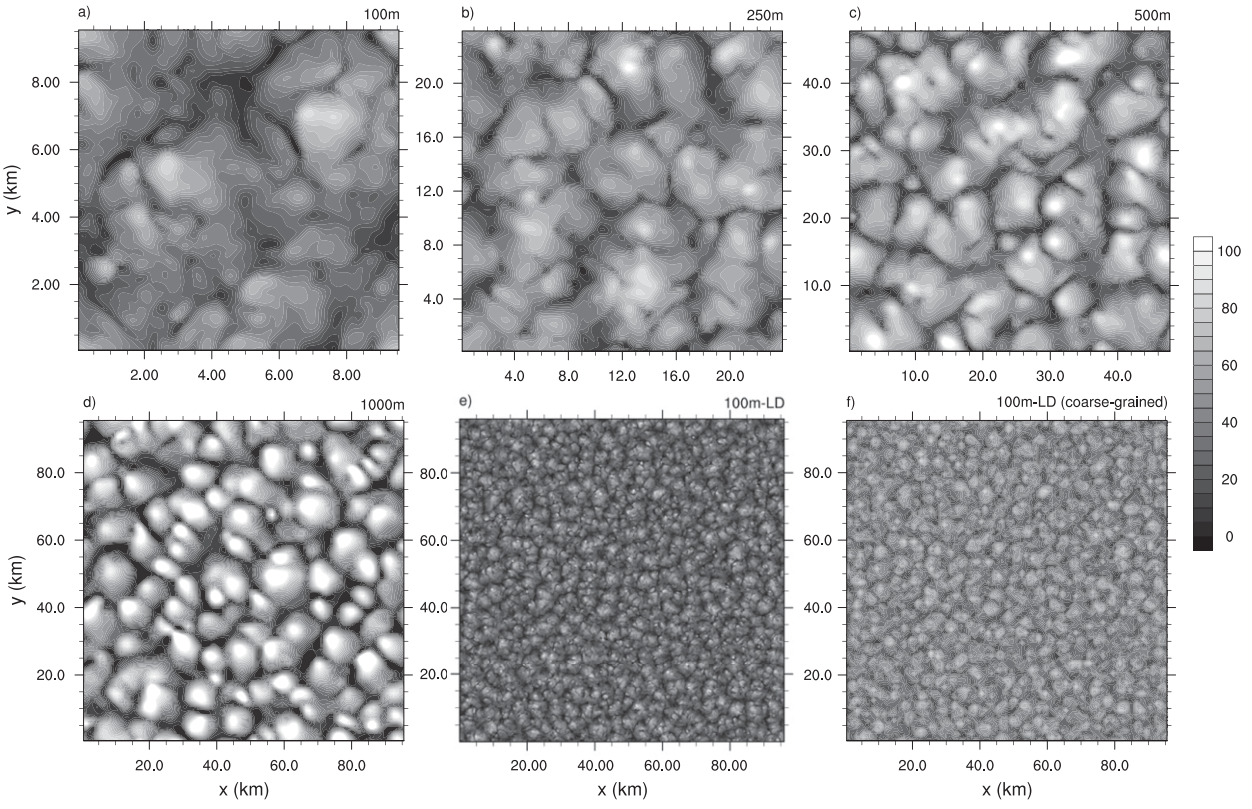

FIG. 15. Snapshots of LWP (g m^{-2}) of simulations using the DRM-Pr turbulence scheme. Vertical spacing is 20 m for all, but different horizontal resolutions are used: (a) 100, (b) 250, (c) 500, (d) 1000, (e)100 (LD), and (f) 100 m [LD, coarse grained onto the 1000-m grid of (d)]. LD denotes the large-domain simulations with horizontal number of grid cells $n_x = n_y = 960$. All others have $n_x = n_y = 96$. Coarse-graining for (f) is done by Fourier-transforming data in (e), removing high-wavenumber modes, and then transforming remaining low-wavenumber modes back onto the coarser, 1000-m grid.

$\Delta z = 20$ m and $\Delta x = \Delta y = 100$ m. DRM-Pr is used for the turbulence closure. The spectrum of w variance in this simulation is computed for this estimation [the spatial scales of other variables' variability tend to grow in simulations until they reach the scale of mesoscale fluctuations (de Roode et al. 2004)]. The w-variance spectrum of this simulation exhibits a peak at about 5 km by the end of the 4-h simulation (Fig. 14). Though the length scale of the peak may grow larger in a longer simulation, 5 km should suffice for the present analysis. Thus, the threshold resolution for TI would be between 6.5 and 16.7 m for the vertical and 156 and 417 m for the horizontal.

In section 3, we showed that when the vertical resolution crosses into the TI, the DRM-Pr still maintains a reasonable cloud layer with $\Delta z = 20$ m, the resolution at which traditional turbulence models fail to maintain the thick, nearly homogeneous cloud layer. DRM-D at 20-m resolution also loses too much cloud water, so it is not appropriate for the TI-zone test. Here, we fix vertical grid spacing at 20 m and test the performance of DRM-Pr, TKE, and SM with different horizontal grid spacings ranging from 100 m to 1 km. The number of grid points is the same, 96 in both x and y directions, for all these simulations; thus, the domain size varies with resolution. Results of these simulations are compared with the large-domain (LD; 96 km $\times$ 96 km) simulations.

The spectra of w variance in the boundary layer as a function of horizontal wavenumbers are shown in Fig. 14 for the simulations using DRM-Pr. As grid spacing increases, variance shifts toward low-wavenumber modes, while the variance in high-wavenumber modes disappears. The spectrum for the 1-km simulation peaks at about 12 km while that for the 100-m simulation peaks at about 5 km. This misrepresentation of the spectra is unavoidable, because as resolution coarsens, the spatial organization of clouds becomes erroneous. As shown in Fig. 15, the organization of the clouds changes with resolution. The clouds in the coarse-resolution runs are organized as larger patches than in the 100-m, large-domain simulation. Even when the LWP field from the large-domain, 100-m-resolution simulation (Fig. 15e)

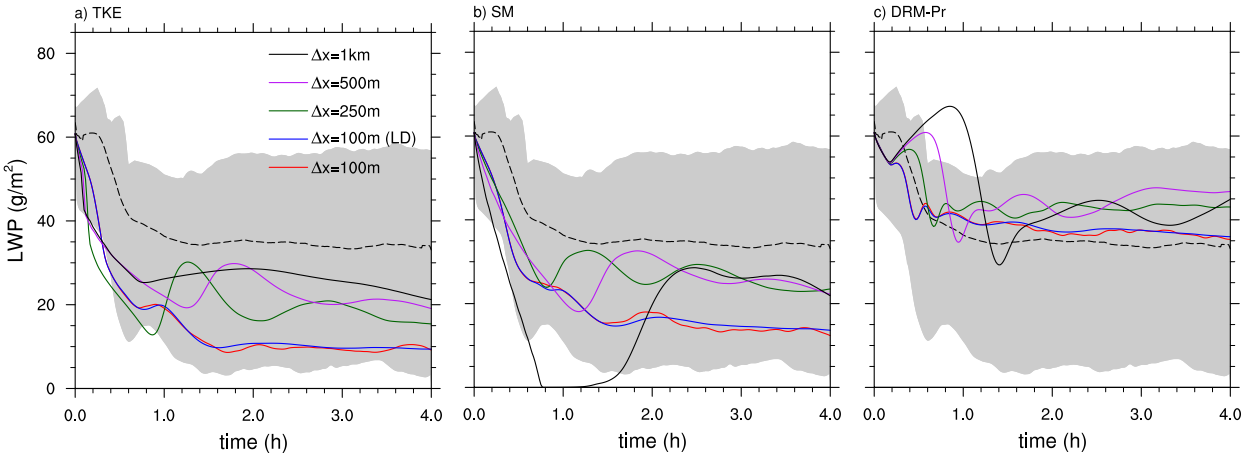

FIG. 16. LWP of simulations using different turbulence closure schemes. Vertical spacing is 20 m for all, but different horizontal resolutions are used. LD denotes the large-domain simulations with horizontal number of grid cells $n_x = n_y = 960$. All others have $n_x = n_y = 96$.

are coarse grained into a coarser 1 km × 1 km grid (Fig. 15f), the difference in cloud cell size between the fine- and coarse-resolution simulations (Figs. 15d,f) is still noticeable. All the DRM-Pr simulations in Fig. 15, however, have nearly 100% cloud cover. Maintaining the correct bulk properties of clouds and boundary layer (e.g., the boundary layer depth) appears to be the only reasonable goal for simulations in the TI zone.

Figure 16 examines the dependence of LWP on horizontal resolution in the simulations with different turbulence closure schemes. Overall, TKE and SM produce much less cloud water than the DRM-Pr simulation. The SM simulation at 1-km resolution even has a short period when all clouds disappear during its spinup. Large-domain and small-domain simulations with the same 100-m horizontal grid spacing show little difference regarding LWP. This insensitivity to domain size is consistent with the previous study by Pedersen et al. (2016). Our integrations are relatively short (4 h), so it is unknown whether domain-size sensitivity may become significant in longer simulations in which large-scale variability is allowed to fully develop. Interestingly, the simulations with coarser horizontal resolutions exhibit more liquid water than the fine, 100-m-resolution simulations. Pedersen et al. (2016) suggest this is because the horizontally coarsened grid dampens vertical velocity fluctuations and mimics anisotropic eddies in the cloud.

Figure 17 further compares the mean profiles of total water mixing ratio in the simulations. TKE and SM exhibit discernible decoupling of the boundary layer, in which total water increases with height for all resolutions shown in Fig. 17. In contrast, DRM-Pr maintains a coupled SCBL, in which total water mixing ratio is uniformly distributed except very close to the surface. Mean profiles of liquid water potential temperature (not shown) also suggest the same difference between DRM-Pr and the other two turbulence models. All of the simulations show weak dependence on resolution. Therefore, if the horizontally averaged properties of the SCBL, such as cloud water, total water, and potential temperature, are the main concerns of an LES, the performance of DRM-Pr in the TI zone is promising. Specifically for this case of the SCBL, anisotropic grid, 500-m–1-km horizontal spacing and 20-m vertical spacing, and the use of DRM-Pr is recommended for TI-zone simulations.

6. Conclusions

Accurately representing the SCBL has been a long-standing issue in weather and climate models. When a strong, sharp capping inversion exists, many LESs with 5-m vertical spacing in the intercomparison study of Stevens et al. (2005) were not able to adequately reproduce the observed cloud water profile and the coupled structure of boundary layer. All LESs in Stevens et al. (2005) use eddy-viscosity-based turbulence models. The stringent requirement of grid resolution was previously thought to be due to the sensitivity of SCBL to the turbulence mixing at cloud top as entrainment rate determines the bulk budget of heat and moisture of the SCBL (Stevens et al. 2005).

In this work, we simulated the SCBL in CM1 with different turbulence closure models, including both traditional eddy-viscosity-based models and more advanced models using explicit filtering and reconstruction. The new models are found to be very useful in helping the LES maintain a thick, homogeneous cloud layer and a coupled boundary layer. Our results indicate that in addition to reducing spurious cloud-top entrainment, the

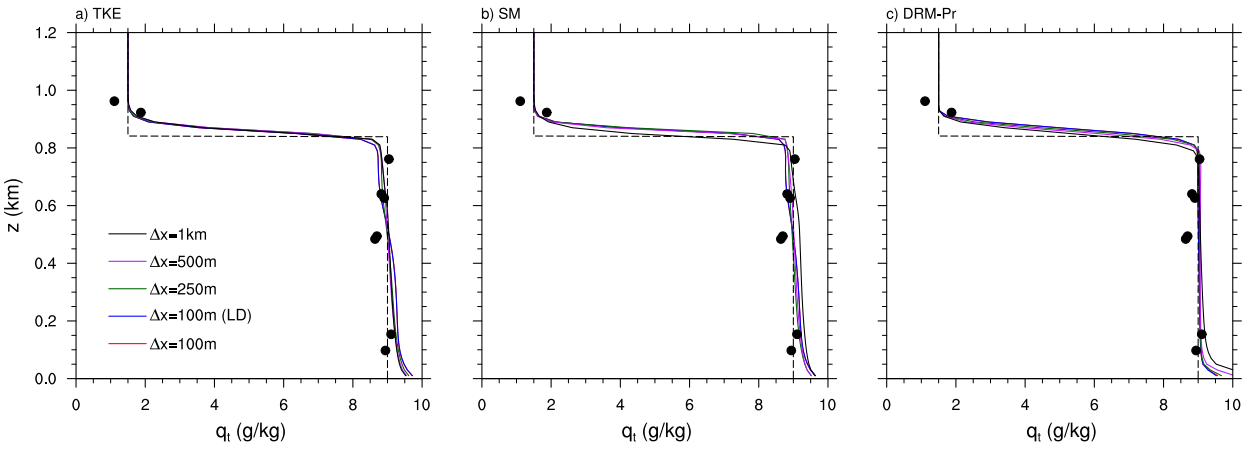

FIG. 17. Mean profiles of total water mixing ratio q_t for the same simulations as those shown in Fig. 16.

representation of energy transfer between resolved and unresolved scales throughout the boundary layer is also important. Because radiative cooling in the upper part of the stratocumulus cloud produces turbulent potential energy (TPE; i.e., buoyancy) in the SCBL and fundamentally drives the resolved turbulence in the boundary layer, correct representation of SFS mixing is critical for maintaining energetic turbulence. The interaction between turbulence and radiation near the sharp capping inversion amplifies the roles played by small-scale eddies and, therefore, the roles of SFS turbulence models (e.g., Stevens et al. 1999). In contrast, important scales of the dry convective boundary layer (CBL) can be well resolved with standard LES resolutions; thus, LES of the dry CBL is less sensitive to turbulence closures than in the SCBL.

Traditional turbulence models rely on the concept of eddy viscosity and only transfer TPE and TKE from resolved scales to smaller unresolved scales. Thus, they often tend to be overly dissipative. For this reason, the 5-m-resolution simulation without a turbulence closure model (NM) exhibits a more realistic SCBL than the simulations at the same resolution and using the traditional eddy-viscosity-based models. In contrast, the DRM can represent backscatter of TPE and TKE, preserving energy at the resolved scales when needed, and therefore maintaining active turbulence throughout the boundary layer while reducing cloud-top entrainment. DRM-D, in which the eddy diffusivity for scalar transport is also computed with dynamic procedures, produces net backscatter of TPE in some regions of the SCBL and maintains the boundary layer with the highest fidelity regarding cloud water amount, temperature profile, and turbulence structure among all simulations at 5-m resolution. An additional set of simulations with the mixed model (MM) for momentum but using the Smagorinsky model only for scalars was performed. Improvements regarding cloud water amount and vertical velocity variance are found in these simulations, implying that improving the representation of the SFS transport of momentum is also key and leads to improvements in and of itself.

Of the two versions of DRM, DRM-D appears to be a more accurate approach at fine resolutions (5-m vertical spacing) than the DRM-Pr, in which eddy diffusivity relies on a parameterized turbulent Prandtl number. When the LES grid mesh is coarsened, however, DRM-D soon fails to maintain the stratocumulus cloud, while DRM-Pr can still maintain a relatively thick cloud layer. This issue is likely due to the explicit stability correction that is included in DRM-Pr but not in DRM-D. At coarse resolutions, local calculations of the dynamic coefficient for subgrid scalar transport in DRM-D lead to spuriously large cloud-top mixing. Including stability dependency in the dynamic model part of the DRM-D could potentially reduce this dependence of DRM-D on grid spacing, as suggested by Kirkpatrick et al. (2006), who used a dynamic Smagorinsky model with stability dependence in their simulations. Ironically, when Wong and Lilly (1994) developed the dynamic eddy-viscosity model utilized in the DRM-D, their purpose was to avoid the troublesome buoyancy dependence and to simplify the dynamic procedure. We will explore the need for a dynamic method with stability corrections for scalar transport in our future investigations.

The advantages of DRM are apparent at the fine resolutions at which most energetic eddies are well resolved but can also be seen in the terra incognita (TI) of numerical simulations. When 20-m vertical and even 1-km horizontal grid spacings are used, the LES using DRM-Pr as its turbulence closure can still maintain a

well-mixed boundary layer with reasonable amounts of cloud water. It is significantly better than the simulations using the same resolution and the traditional eddy-viscosity-based turbulence closures, which exhibit less cloud water and a boundary layer with slight warming biases. The detailed structures of boundary layer motions are distorted as resolution is coarsened, which is not avoidable, but the bulk properties of the SCBL, which is the concern in weather- and climate-focused studies, are well captured by the TI-zone simulations using DRM-Pr.

A delicate issue not addressed thoroughly in this study is the interaction between the explicit turbulent fluxes due to SFS turbulence models and the implicit mixing inherent in dissipative numerical schemes. WENO schemes produce numerical diffusion in the flow, which may be very strong near the capping inversion because of the presence of sharp gradients. Thus, in our simulations, which use the WENO scheme for both momentum and scalar advection, the exact entrainment in the cloud-top region is likely determined by both the SFS models and numerical diffusion, in addition to the resolved motions. Pressel et al. (2017) demonstrated that changing advection schemes alone can dramatically change the quality of simulations for the DYCOMS RF01 case. Our results here may not hold for some choices of numerical schemes, though we briefly explored fifth- and sixth-order schemes, as discussed in section 2b. A detailed investigation of the interaction between the implicit numerical diffusion and explicit turbulence model mixing is beyond the scope of this study.

The stratocumulus-capped boundary layer under strong, sharp inversion is a challenging regime for LES. DRM can model backscatter through its reconstructed RSFS stresses and fluxes and thus provide an SCBL with higher fidelity in the simulations compared with traditional eddy-viscosity-based models. At typical LES resolution, DRM-D, the DRM that computes a dynamic eddy diffusivity, is recommended because it can maximize the effects of backscatter modeled by reconstruction. When the resolution falls into the TI zone of numerical simulations, DRM-Pr, the DRM model using a parameterized Prandtl number to compute eddy diffusivity, is preferred, because it can suppress spurious scalar mixing under stable conditions through the parameterization of the Prandtl number while still allowing backscatter to be modeled by reconstruction.

Acknowledgments. The authors thank three anonymous reviewers for their helpful reviews. This research was supported by National Science Foundation (NSF) Grants AGS-1503860 and AGS-1503885. We would like to acknowledge high-performance computing support from Yellowstone (ark:/85065/d7wd3xhc) provided by NCAR's Computational and Information Systems Laboratory, which is sponsored by the NSF.

APPENDIX

Higher-Order Reconstruction

This appendix examines the impact of higher-order reconstruction, for which we use the approximate deconvolution method (ADM) and three-dimensional explicit filters. We focus on DRM-Pr because of its superior performance at coarse resolutions (compared to DRM-D, which has no stability correction). The resolvable subfilter-scale (RSFS) model of the dynamic reconstruction model (DRM) relies on knowledge of the resolved flow alone, and in theory, the reconstruction can reproduce the spectra up to the filter-width cutoff frequency (Carati et al. 2001; Chow et al. 2005). Although not shown here, examination of the components of the reconstructed velocity $\tilde{u}^*$ and potential temperature $\tilde{\theta}^*$ shows that the correction at each higher level decreases monotonically and rapidly in general (unless, for example, the numerical integration stencil covers areas of rapid underresolved gradients; cf. Chow 2004, sections 5.3 and 5.4).

We present three figures to illustrate the effects of higher-order reconstruction. Figures A1 and A2 parallel Figs. 1 and 7, in which the horizontal grid size is held at 35 m and the vertical resolution is varied. In Fig. A3 (cf. Fig. 16), the vertical spacing is held at 20 m, and the horizontal spacing is varied. Figure A1 shows liquid water path (LWP) time series from a set of DRM-Pr simulations. For fixed horizontal resolution, the vertical grid spacing Δz ranges from 5 to 40 m. Increasing the order of reconstruction brings some improvement. With $\Delta z = 5$ m, the LWP exhibits small improvements as reconstruction order increases from 1 to 5. The simulation with 40-m vertical spacing, however, is limited by its very coarse resolution and still significantly underpredicts LWP even when fifth-order reconstruction is used.

Figure A2 shows the mean profiles of resolved w variance. Increasing the order of reconstruction brings noticeable improvement. Figure A2 also shows that above the cloud top, higher-order reconstruction can induce artificial turbulence in the resolved flow. While the simulations with higher resolutions ($\Delta z = 5$ and 10 m) do not exhibit significant vertical motions above the cloud top, the simulations with coarse vertical

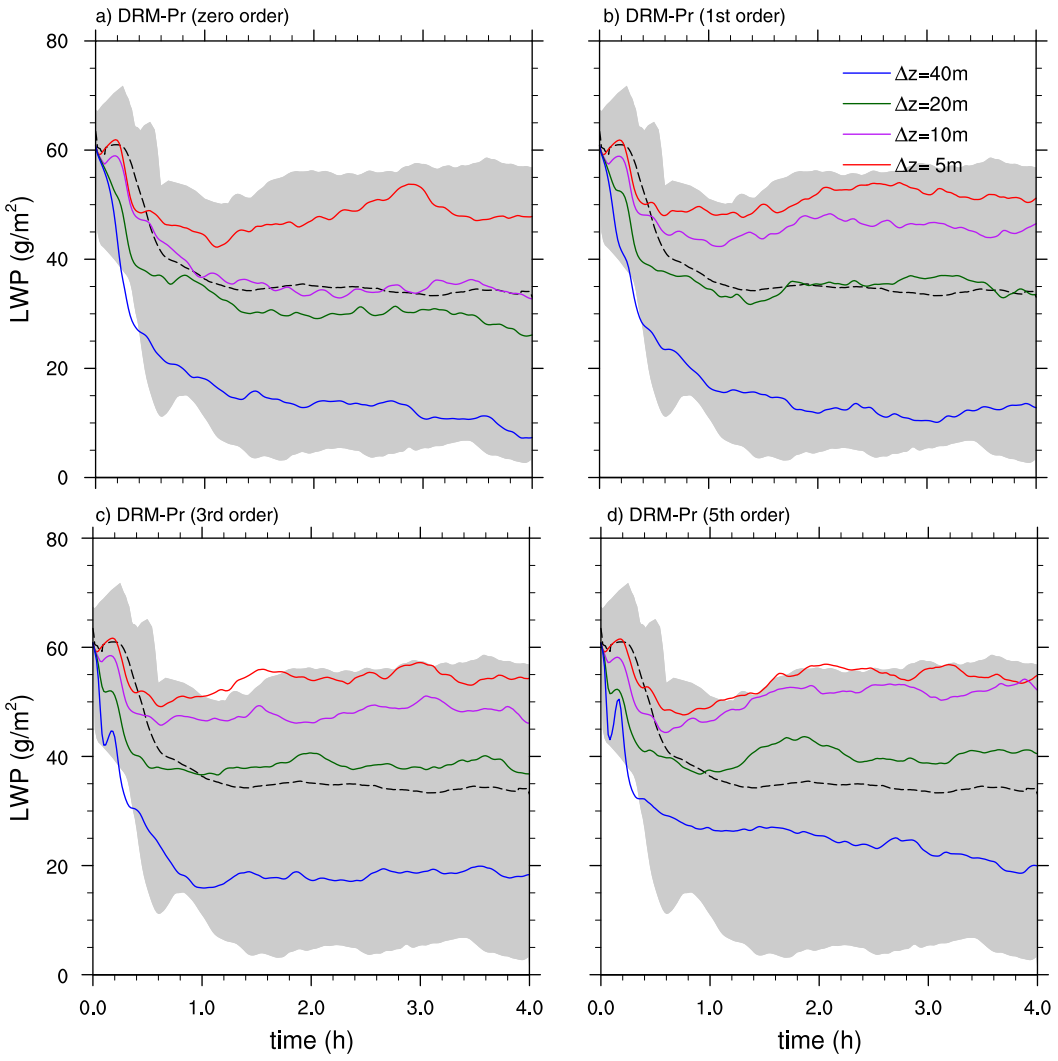

FIG. A1. LWP time series for the DRM-Pr simulations with (a) zero-, (b) first-, (c) third-, and (d) fifth-order reconstruction. Horizontal grid spacing for these simulations is fixed at 35 m, while the vertical resolution is varied from 5 to 40 m.

resolutions show nonzero variance for the resolved vertical velocity. This problem is particularly prominent for the simulations with $\Delta z = 40$ m, and the amplitude of artificial turbulence increases with the order of reconstruction. This suggests that artificial mixing may be produced by the high-order reconstruction at this insufficient resolution. Higher-order reconstruction requires repeated application of the explicit filter [see Eq. (11)] and thus effectively uses a wider stencil to reconstruct a variable. For example, the fifth-order reconstruction involves 11 grid cells in each direction. Thus, at coarse resolutions, the turbulent state of a variable below the inversion can affect the reconstructed fluxes in the stable layer above the inversion, leading to spurious mixing.

In Figure A3, the effects of high-order reconstruction are evaluated for TI-resolution simulations. These runs parallel the simulations in section 5 (Fig. 16), where the vertical resolution is fixed at 20 m and the horizontal grid spacing ranges from 100 to 1000 m. Figure A3 shows that increasing the order of reconstruction increases LWP and thus can improve simulations of the stratocumulus-capped boundary layer (SCBL). The LWP of the simulations with very coarse horizontal resolutions ($\Delta x = 500$ and 1000 m), however, appears to be growing unrealistically fast; thus, the fifth-order reconstruction may not be reliable because of the effect of numerical errors in the series expansion at poor resolution. These TI simulations do not exhibit significant artificial turbulence above the cloud top in their w-variance

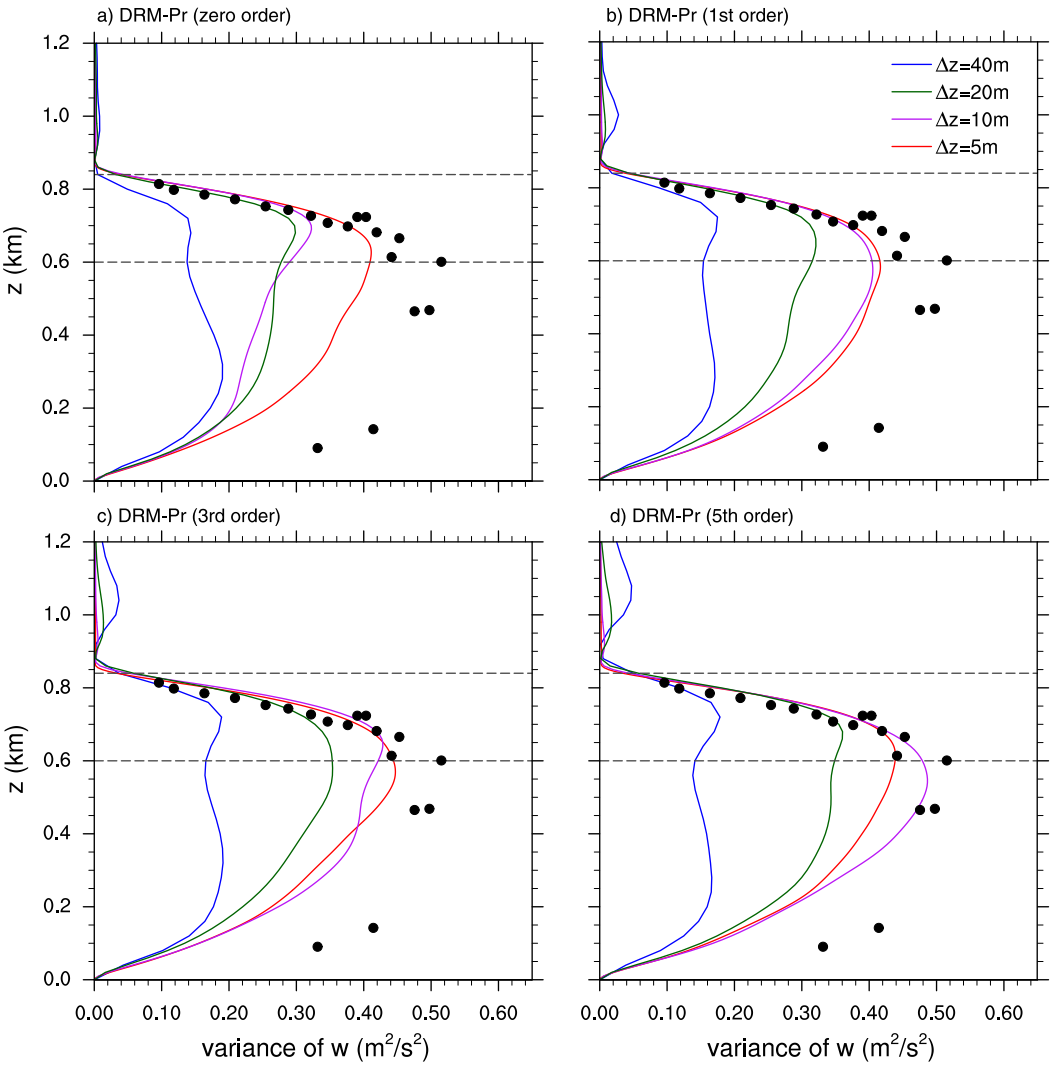

FIG. A2. Hour-4 mean w variance $\langle \overline{w}'\overline{w}' \rangle$ for the DRM-Pr simulations with (a) zero-, (b) first-, (c) third-, and (d) fifth-order reconstruction. Horizontal grid spacing for these simulations is fixed at 35 m, while vertical resolution is varied from 5 to 40 m.

profiles (not shown), probably because their large grid aspect ratios damp vertical motions to some extent.

The impact of zero-order (one term) reconstruction is significant and positive as shown in the main body of the paper. Generally, increasing the order of reconstruction, beyond zero order, is beneficial, but the effect is small overall and can lead to spurious mixing at very coarse resolutions. Meanwhile, increasing the reconstruction by one order can lead to about a 4% increase in Cloud Model 1 (CM1)'s computing time (Table 1). Thus, the computational cost of significantly increasing reconstruction outweighs the benefits, and in some cases, particularly with insufficient resolution and sharp gradients in the flow, artificial mixing may appear in the simulations. In a mathematical sense, high-order reconstruction is sensitive because the inverse filtering is equivalent to solving a Fredholm integral equation of the first kind, which is inherently an ill-posed problem. This means its solution is very sensitive to small-amplitude noise in the system, which can in particular be introduced when operating near the Nyquist limit of the grid and with sharp gradients in the flow field (Hansen 1992). Accordingly, and consistent with Chow et al. (2005), zero-order reconstruction is likely adequate for most situations, and we generally recommend the use of low-order ($\leq$3) reconstruction in the DRM.

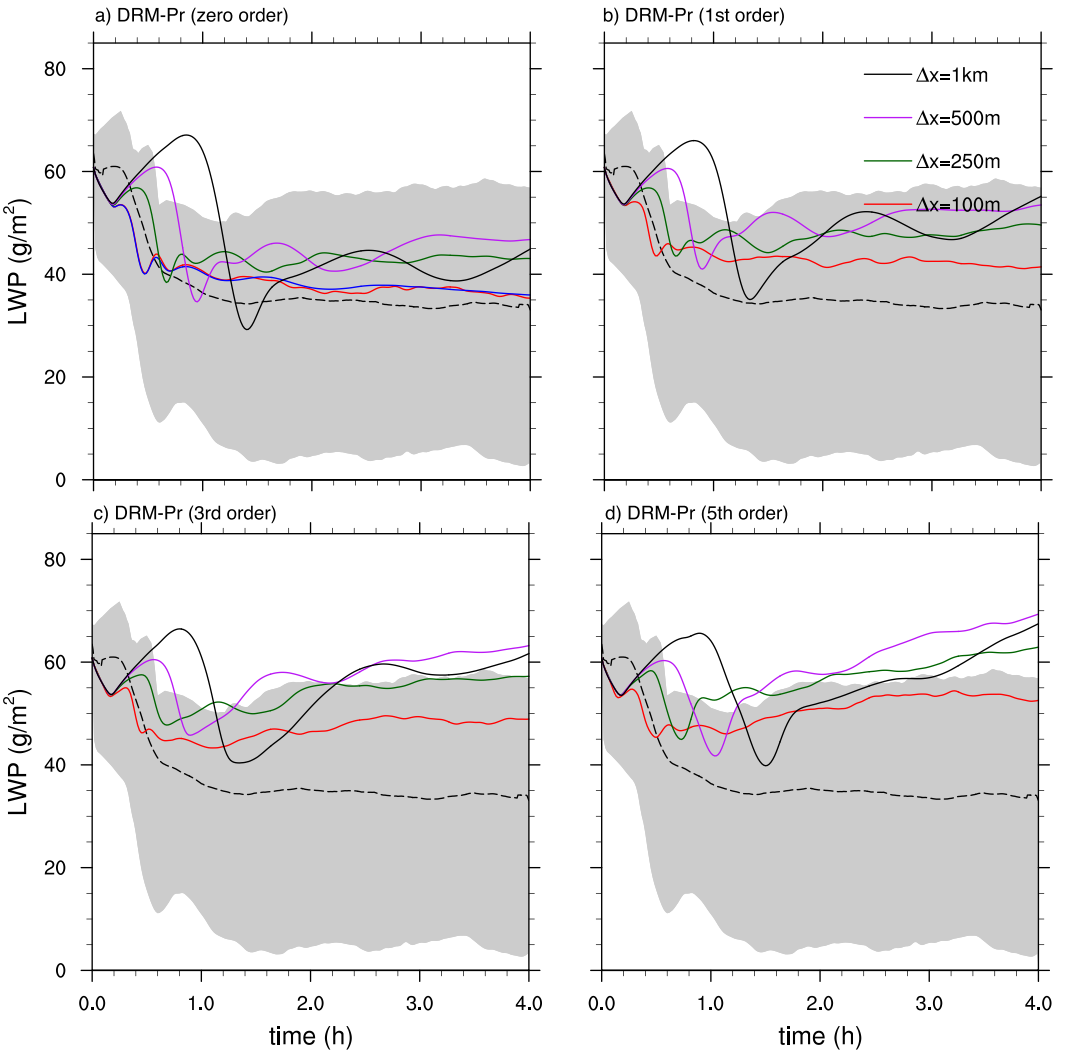

FIG. A3. LWP time series for the DRM-Pr simulations with (a) zero-, (b) first-, (c) third-, and (d) fifth-order reconstruction. Vertical grid spacing for these simulations is fixed at 20 m, while the horizontal resolution is varied from 100 to 1000 m.

REFERENCES

Bardina, J., J. H. Ferziger, and W. C. Reynolds, 1983: Improved turbulence models based on large eddy simulation of homogeneous, incompressible, turbulent flows. Stanford University Dept. of Mechanical Engineering Tech. Rep. TF-19, 175 pp.

Basu, S., and F. Porté-Agel, 2006: Large-eddy simulation of stably stratified atmospheric boundary layer turbulence: A scale-dependent dynamic modeling approach. *J. Atmos. Sci.*, **63**, 2074–2091, https://doi.org/10.1175/JAS3734.1.

Borges, R., M. Carmona, B. Costa, and W. S. Don, 2008: An improved weighted essentially non-oscillatory scheme for hyperbolic conservation laws. *J. Comput. Phys.*, **227**, 3191–3211, https://doi.org/10.1016/j.jcp.2007.11.038.

Bretherton, C. S., 2015: Insights into low-latitude cloud feedbacks from high-resolution models. *Philos. Trans. Roy. Soc. London*, **373A**, 20140415, https://doi.org/10.1098/rsta.2014.0415.

——, and P. N. Blossey, 2014: Low cloud reduction in a greenhouse-warmed climate: Results from Lagrangian LES of a subtropical marine cloudiness transition. *J. Adv. Model. Earth Syst.*, **6**, 91–114, https://doi.org/10.1002/2013MS000250.

——, and Coauthors, 1999: An intercomparison of radiatively driven entrainment and turbulence in a smoke cloud, as simulated by different numerical models. *Quart. J. Roy. Meteor. Soc.*, **125**, 391–423, https://doi.org/10.1002/qj.49712555402.

Brown, A. R., J. Hobson, and N. Wood, 2001: Large-eddy simulation of neutral turbulent flow over rough sinusoidal ridges. *Bound.-Layer Meteor.*, **98**, 411–441, https://doi.org/10.1023/A:1018703209408.

Bryan, G. H., and J. M. Fritsch, 2002: A benchmark simulation for moist nonhydrostatic numerical models. *Mon. Wea. Rev.*, **130**, 2917–2928, https://doi.org/10.1175/1520-0493(2002)130<2917:ABSFMN>2.0.CO;2.

——, and R. Rotunno, 2009: The maximum intensity of tropical cyclones in axisymmetric numerical model simulations.

Mon. Wea. Rev., **137**, 1770–1789, https://doi.org/10.1175/2008MWR2709.1.

Carati, D., G. S. Winckelmans, and H. Jeanmart, 2001: On the modelling of the subgrid-scale and filtered-scale stress tensors in large-eddy simulation. *J. Fluid Mech.*, **441**, 119–138, https://doi.org/10.1017/S0022112001004773.

Cheng, A., and K.-M. Xu, 2008: Simulation of boundary-layer cumulus and stratocumulus clouds using a cloud-resolving model with low- and third-order turbulence closures. *J. Meteor. Soc. Japan*, **86A**, 67–86, https://doi.org/10.2151/jmsj.86A.67.

——, ——, and B. Stevens, 2010: Effects of resolution on the simulation of boundary-layer clouds and the partition of kinetic energy to subgrid scales. *J. Adv. Model. Earth Syst.*, **2** (1), https://doi.org/10.3894/JAMES.2010.2.3.

Chow, F. K., 2004: Subfilter-scale turbulence modeling for large-eddy simulation of the atmospheric boundary layer over complex terrain. Ph.D. dissertation, Stanford University, 339 pp.

——, and P. Moin, 2003: A further study of numerical errors in large-eddy simulations. *J. Comput. Phys.*, **184**, 366–380, https://doi.org/10.1016/S0021-9991(02)00020-7.

——, R. L. Street, M. Xue, and J. H. Ferziger, 2005: Explicit filtering and reconstruction turbulence modeling for large-eddy simulation of neutral boundary layer flow. *J. Atmos. Sci.*, **62**, 2058–2077, https://doi.org/10.1175/JAS3456.1.

Computational and Information Systems Laboratory, 2012: Yellowstone: IBM iDataPlex System. National Center for Atmospheric Research, http://n2t.net/ark:/85065/d7wd3xhc.

Deardorff, J. W., 1980: Stratocumulus-capped mixed layers derived from a three-dimensional model. *Bound.-Layer Meteor.*, **18**, 495–527, https://doi.org/10.1007/BF00119502.

de Lozar, A., and J. P. Mellado, 2015: Mixing driven by radiative and evaporative cooling at the stratocumulus top. *J. Atmos. Sci.*, **72**, 4681–4700, https://doi.org/10.1175/JAS-D-15-0087.1.

de Roode, S. R., P. G. Duynkerke, and H. J. Jonker, 2004: Large-eddy simulation: How large is large enough? *J. Atmos. Sci.*, **61**, 403–421, https://doi.org/10.1175/1520-0469(2004)061<0403:LSHLIL>2.0.CO;2.

Dufresne, J.-L., and S. Bony, 2008: An assessment of the primary sources of spread of global warming estimates from coupled atmosphere–ocean models. *J. Climate*, **21**, 5135–5144, https://doi.org/10.1175/2008JCLI2239.1.

Gullbrand, J., and F. K. Chow, 2003: The effect of numerical errors and turbulence models in large-eddy simulations of channel flow, with and without explicit filtering. *J. Fluid Mech.*, **495**, 323–341, https://doi.org/10.1017/S0022112003006268.

Hansen, P. C., 1992: Numerical tools for analysis and solution of Fredholm integral equations of the first kind. *Inverse Probl.*, **8**, 849–872, https://doi.org/10.1088/0266-5611/8/6/005.

Jones, C. R., C. S. Bretherton, and P. N. Blossey, 2014: Fast stratocumulus time scale in mixed layer model and large eddy simulation. *J. Adv. Model. Earth Syst.*, **6**, 206–222, https://doi.org/10.1002/2013MS000289.

Katopodes, F. V., R. L. Street, and J. H. Ferziger, 2000: A theory for the subfilter-scale model in large-eddy simulation. Stanford University Environmental Fluid Mechanics Laboratory Tech. Rep. 2000-K1, 22 pp.

Kirkpatrick, M. P., A. S. Ackerman, D. E. Stevens, and N. N. Mansour, 2006: On the application of the dynamic Smagorinsky model to large-eddy simulations of the cloud-topped atmospheric boundary layer. *J. Atmos. Sci.*, **63**, 526–546, https://doi.org/10.1175/JAS3651.1.

Larson, V. E., D. P. Schanen, M. Wang, M. Ovchinnikov, and S. Ghan, 2012: PDF parameterization of boundary layer clouds in models with horizontal grid spacings from 2 to 16 km. *Mon. Wea. Rev.*, **140**, 285–306, https://doi.org/10.1175/MWR-D-10-05059.1.

Leslie, D. C., and G. L. Quarini, 1979: The application of turbulence theory to the formulation of subgrid modelling procedures. *J. Fluid Mech.*, **91**, 65–91, https://doi.org/10.1017/S0022112079000045.

Mason, P. J., 1985: A numerical study of cloud streets in the planetary boundary layer. *Bound.-Layer Meteor.*, **32**, 281–304, https://doi.org/10.1007/BF00121884.

——, and D. Thomson, 1992: Stochastic backscatter in large-eddy simulations of boundary layers. *J. Fluid Mech.*, **242**, 51–78, https://doi.org/10.1017/S0022112092002271.

Matheou, G., and D. Chung, 2014: Large-eddy simulation of stratified turbulence. Part II: Application of the stretched-vortex model to the atmospheric boundary layer. *J. Atmos. Sci.*, **71**, 4439–4460, https://doi.org/10.1175/JAS-D-13-0306.1.

Mellado, J. P., 2017: Cloud-top entrainment in stratocumulus clouds. *Annu. Rev. Fluid Mech.*, **49**, 145–169, https://doi.org/10.1146/annurev-fluid-010816-060231.

Moeng, C.-H., P. Sullivan, M. Khairoutdinov, and D. Randall, 2010: A mixed scheme for subgrid-scale fluxes in cloud-resolving models. *J. Atmos. Sci.*, **67**, 3692–3705, https://doi.org/10.1175/2010JAS3565.1.

O'Neill, J., X.-M. Cai, and R. Kinnersley, 2015: Improvement of a stochastic backscatter model and application to large-eddy simulation of street canyon flow. *Quart. J. Roy. Meteor. Soc.*, **142**, 1121–1132, https://doi.org/10.1002/qj.2715.

Pedersen, J. G., S. P. Malinowski, and W. W. Grabowski, 2016: Resolution and domain-size sensitivity in implicit large-eddy simulation of the stratocumulus-topped boundary layer. *J. Adv. Model. Earth Syst.*, **8**, 885–903, https://doi.org/10.1002/2015MS000572.

Pope, S. B., 2000: *Turbulent Flows.* Cambridge University Press, 802 pp.

Pressel, K. G., S. Mishra, T. Schneider, C. M. Kaul, and Z. Tan, 2017: Numerics and subgrid-scale modeling in large eddy simulations of stratocumulus clouds. *J. Adv. Model. Earth Syst.*, **9**, 1342–1365, https://doi.org/10.1002/2016MS000778.

Smagorinsky, J., 1963: General circulation experiments with the primitive equations: I. The basic experiment. *Mon. Wea. Rev.*, **91**, 99–164, https://doi.org/10.1175/1520-0493(1963)091<0099:GCEWTP>2.3.CO;2.

Stevens, B., C.-H. Moeng, and P. P. Sullivan, 1999: Large-eddy simulations of radiatively driven convection: Sensitivities to the representation of small scales. *J. Atmos. Sci.*, **56**, 3963–3984, https://doi.org/10.1175/1520-0469(1999)056<3963:LESORD>2.0.CO;2.

——, and Coauthors, 2003: On entrainment rates in nocturnal marine stratocumulus. *Quart. J. Roy. Meteor. Soc.*, **129**, 3469–3493, https://doi.org/10.1256/qj.02.202.

——, and Coauthors, 2005: Evaluation of large-eddy simulations via observations of nocturnal marine stratocumulus. *Mon. Wea. Rev.*, **133**, 1443–1462, https://doi.org/10.1175/MWR2930.1.

Stolz, S., and N. A. Adams, 1999: An approximate deconvolution procedure for large-eddy simulation. *Phys. Fluids*, **11**, 1699–1701, https://doi.org/10.1063/1.869867.

——, ——, and L. Kleiser, 2001: An approximate deconvolution model for large-eddy simulation with application to incompressible wall-bounded flows. *Phys. Fluids*, **13**, 997–1015, https://doi.org/10.1063/1.1350896.

Venayagamoorthy, S. K., and D. D. Stretch, 2010: On the turbulent Prandtl number in homogeneous stably stratified turbulence. *J. Fluid Mech.*, **644**, 359–369, https://doi.org/10.1017/S002211200999293X.

Wilson, J. M., and S. K. Venayagamoorthy, 2015: A shear-based parameterization of turbulent mixing in the stable atmospheric boundary layer. *J. Atmos. Sci.*, **72**, 1713–1726, https://doi.org/10.1175/JAS-D-14-0241.1.

Wong, V. C., and D. K. Lilly, 1994: A comparison of two dynamic subgrid closure methods for turbulent thermal convection. *Phys. Fluids*, **6**, 1016–1023, https://doi.org/10.1063/1.868335.

Wyant, M. C., C. S. Bretherton, H. A. Rand, and D. E. Stevens, 1997: Numerical simulations and a conceptual model of the stratocumulus to trade cumulus transition. *J. Atmos. Sci.*, **54**, 168–192, https://doi.org/10.1175/1520-0469(1997)054<0168:NSAACM>2.0.CO;2.

Wyngaard, J. C., 2004: Toward numerical modeling in the ''terra incognita.'' *J. Atmos. Sci.*, **61**, 1816–1826, https://doi.org/10.1175/1520-0469(2004)061<1816:TNMITT>2.0.CO;2.

Xiao, H., and Coauthors, 2015: Modifications to WRF's dynamical core to improve the treatment of moisture for large-eddy simulations. *J. Adv. Model. Earth Syst.*, **7**, 1627–1642, https://doi.org/10.1002/2015MS000532.

Zang, Y., R. L. Street, and J. R. Koseff, 1993: A dynamic mixed subgrid-scale model and its application to turbulent recirculating flows. *Phys. Fluids*, **5**, 3186–3196, https://doi.org/10.1063/1.858675.

Zelinka, M. D., S. A. Klein, K. E. Taylor, T. Andrews, M. J. Webb, J. M. Gregory, and P. M. Forster, 2013: Contributions of different cloud types to feedbacks and rapid adjustments in CMIP5. *J. Climate*, **26**, 5007–5027, https://doi.org/10.1175/JCLI-D-12-00555.1.

Zilitinkevich, S. S., T. Elperin, N. Kleeorin, and I. Rogachevskii, 2007: Energy- and flux-budget (EFB) turbulence closure model for stably stratified flows. Part I: Steady-state, homogeneous regimes. *Bound.-Layer Meteor.*, **125**, 167–191, https://doi.org/10.1007/s10546-007-9189-2.